remote sensing

MDPI

Article

Meteorological Changes Across Curiosity Rover's Traverse Using REMS Measurements and Comparisons Between Measurements and MRAMS Model Results

María Ruíz [1,*], Eduardo Sebastián-Martínez [1], Jose Antonio Rodríguez-Manfredi [1], Jorge Pla-García [1], Manuel de la Torre-Juarez [2] and Scot C. R. Rafkin [3]

[1] Centro de Astrobiología (CAB), INTA-CSIC, 28850 Madrid, Spain; sebastianme@cab.inta-csic.es (E.S.-M.); manfredi@cab.inta-csic.es (J.A.R.-M.); jpl2@cab.inta-csic.es (J.P.-G.)
[2] Jet Propulsion Laboratory, California Institute of Technology, Pasadena, CA 91109, USA; manuel.delatorrejuarez@jpl.nasa.gov
[3] Southwest Research Institute, Boulder, CO 80302, USA; scot.rafkin@swri.org
* Correspondence: mruiz@cab.inta-csic.es

Abstract: The Curiosity rover, from NASA's Mars Science Laboratory (MSL), has climbed nearly 740 m from its landing location at −4500.971 m in Gale Crater to a location reached on sol 3967 on the slopes of Mt. Sharp at −3765.27 m. We examine the atmospheric pressure, surface and atmospheric temperatures, relative humidity, and water vapor volume mixing ratios from measurements made by the Rover Environmental Monitoring Station (REMS), taken along the trajectory traveled over 3967 sols spanning from late MY31 to mid-MY37, on an interannual scale. The results help us understand the Martian meteorology inside Gale Crater. The atmospheric pressure and temperature changes caused by the elevation variation of the rover show the impact of the altitude change on the atmospheric dynamics. Regarding the rover's locations for MY32 and MY36, a detailed comparative analysis of the full diurnal cycle is performed for the solstices and equinoxes. These scenarios are examined using the REMS and the Mars Regional Atmospheric Modeling System (MRAMS) data. We compare the REMS and MRAMS data to evaluate their concordance. We present, for the first time, a hypothesis for the existence of the cold pool phenomenon, which also occurs on Earth, based on REMS data.

Keywords: Mars; meteorology; atmosphere

check for updates

Academic Editor: Roberto Orosei

Received: 2 December 2024
Revised: 5 January 2025
Accepted: 15 January 2025
Published: 22 January 2025

Citation: Ruíz, M.; Sebastián-Martínez, E.; Rodríguez-Manfredi, J.A.; Pla-García, J.; de la Torre-Juarez, M.; Rafkin, S.C.R. Meteorological Changes Across Curiosity Rover's Traverse Using REMS Measurements and Comparisons Between Measurements and MRAMS Model Results. *Remote Sens.* **2025**, *17*, 368. https://doi.org/10.3390/rs17030368

Copyright: © 2025 by the authors. Licensee MDPI, Basel, Switzerland. This article is an open access article distributed under the terms and conditions of the Creative Commons Attribution (CC BY) license (https://creativecommons.org/licenses/by/4.0/).

1. Introduction

In the atmosphere of Mars, phenomena also occur that take place in Earth's atmosphere, such as cold pools [1–3], and understanding them is key to studying the atmospheric boundary layer, which on Mars, just like on Earth, is subdivided vertically [4]. This manuscript focuses on the Planetary Atmospheric Boundary Layer (PBL) in and around Gale Crater, particularly in the PBL of the environment, which the Curiosity rover from the MSL mission [5] has been measuring throughout its journey since landing on 6 August 2012 (UTC) at 4.49° S, 137.42° E, in the northwestern part of Gale Crater (Figure 1).

The atmosphere and surface can condition each other, e.g., [6–9]. A change in the altitude can cause significant changes in the atmospheric pressure and temperatures [10,11]. Also, depending on the terrain composition of a site, its altitude, and the year's season, the optimal conditions for atmospheric saturation and condensation have been reported [12]. This work analyzes how Gale Crater's varied mountain topography at nearby locations can lead to different atmospheric dynamics, e.g., [13].

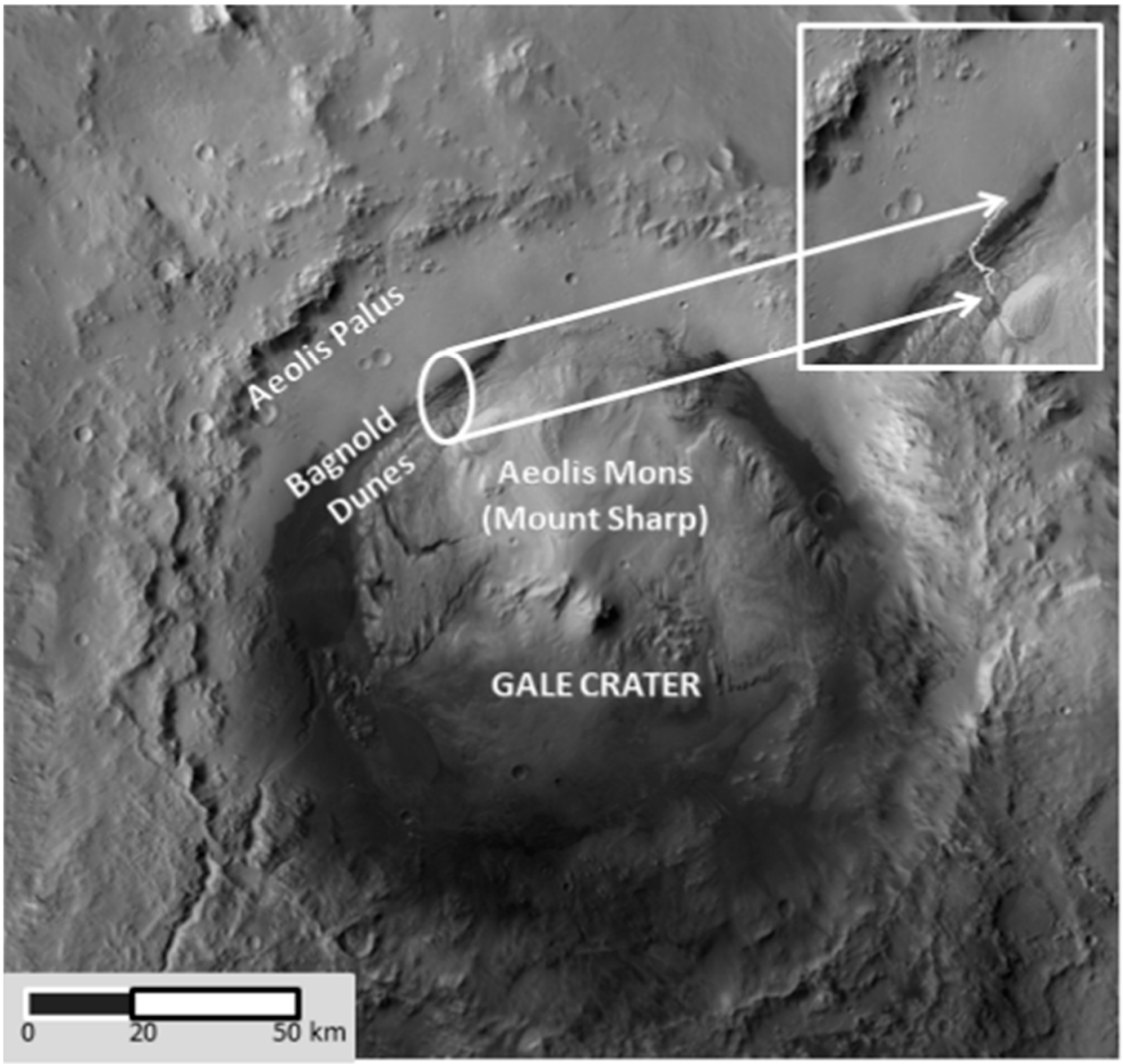


Figure 1. Map of the environment where the MSL Curiosity rover is located. This has been created with image data from the Context and the HiRISE cameras on NASA's Mars Reconnaissance Orbiter. In the enlarged inset panel of the environment, the Curiosity rover's trajectory is shown in white.

The objective of this work is to investigate the atmospheric dynamics, using REMS measurements on daily and seasonal time scales, over the 3967 sols, spanning nearly six of the almost seven Martian years (from late MY31 to early MY37) completed. The rover's ~740 m traverse up the slopes of Mt. Sharp has included some short descents, as seen in Figure 2, which could condition the daily scale fluctuations of some atmospheric magnitudes such as atmospheric pressure and temperature. In addition, this work compares the MRAMS results with the REMS observations in order to look for the concordances that they present. In this sense, it is intended to show the discrepancies between the model and the measurements in order to improve the model in the future. Such discrepancies are larger in scenarios where air turbulence is higher, which could be due to annual events such as increased Hadley cell winds and/or increased CO_2 and dust than at other epochs of the Martian year, something that will be discussed throughout the present work.

This article is structured in the following sections: Section 2 describes the methodology used to obtain the data of the REMS measurements (Section 2.1) and presents the numerical

experiments performed with MRAMS (Section 2.2). Section 3 shows the results and is subdivided into Section 3.1, where the results on an interannual time scale of seasonal variations are shown; Section 3.2 analyzes daily scale processes and a comparison between REMS and MRAMS for the sols of the solar equinoxes and solstices. Section 4 presents the analysis and discussion of the results with interannual evolution (Section 4.1) and on the mesoscale together with detections of improvements in MRAMS (Section 4.2). Section 5 presents a summary and the conclusions.

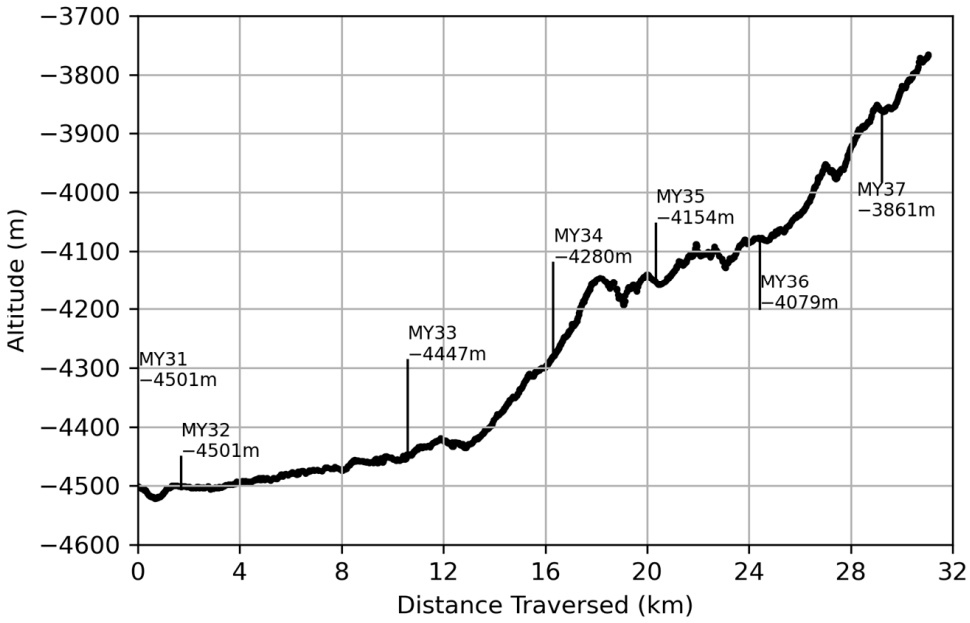


Figure 2. Curiosity rover trajectory defined from altitude versus distance traveled on the surface. The beginning of each year (except MY31) is indicated by text on the image along with the altitude reached by the rover at that point in its trajectory and the altitude at which the year begins. The initiation of year 31 refers to the start of the rover's mission.

2. Data and Methodology

In this work, we use measurements by the REMS's instruments (Section 2.1) and model air temperature and pressure values for a typical sol from MRAMS (Section 2.2). The timing convention used in this paper is Local Mean Solar Time (LMST). This is the reference frame used for all MSL planning. Hence, all illustrated and quantified results are referred to in this way. All sols are given in MSL sols, with sol 0 being the sol (starting at midnight local time) at the landing site at the time of landing, at Ls = 151°. Ls, solar longitude, describes Mars's position in its orbit around the Sun. The seasons are referred to in terms of Ls. Ls = 0° is northern spring equinox, Ls = 90° is northern summer solstice, Ls = 180° is northern autumn equinox, and Ls = 270° is northern winter solstice.

2.1. REMS Observations

The REMS nominal observation strategy consists of recording observations over 5 min at the beginning of every LMST hour on Mars. During those periods, all REMS sensors measure one sample per second [14,15]. In addition to these 5 min per hour measurements, additional 1 h extended observation blocks (EBs) of REMS can be added to each sol's plan. The strategy for the REMS measurement mode was to add EBs every six hours, advancing one hour each sol, to cover the entire diurnal cycle in 6 sols [14–16]. The REMS sensors used in this research are listed in Table 1.

Table 1. REMS sensors.

Sensor	Observed	Variable	Range	Resolution	Accuracy	Ref.
REMS-GTS	Ground brightness temperature	Tg (K)	150–300	0.1	±5	[17]
REMS-ATS	Atmospheric temperature	Ta (K)	150–300	0.1	±5	[14]
REMS-PS	Atmospheric pressure	P (Pa)	0–1400	0.2	±3.5	[18]
REMS-HS	Relative humidity	RH (%)	0–100	0.1	2% in 0 °C 4% in −40 °C 8% in −70 °C	[19]

Technical parameters of the REMS sensors used in this work. From left to right, the sensor's acronym, the magnitude it measures, the variable symbol, the range in which the sensor measures, and its resolution and precision are shown. The last column, Ref, indicates a bibliographic reference that focuses in detail on the sensor to which it refers.

2.2. MRAMS Experiment Design and Configuration

The Mars Regional Atmospheric Modeling System (MRAMS) mesoscale model [20,21] has been used to compare REMS measurements of atmospheric pressure and temperature. Two different topographic scenarios for the solstices and equinoxes have been simulated with MRAMS. These are the rover locations in MY32 and MY36. For this purpose, two experiments were performed using the same procedure, but their parameterization values differed. Table 2 shows these values for both scenarios, from which the model calculates the temperature and pressure for the solar longitude (Ls) corresponding to each solstice and equinox, considering the topography (Figure 3). Once these values are set in the model, a grid of nested meshes delimits the region of interest. Seven nested grids were used for each scenario, each of which represented the topography, with the last one achieving the best resolution. From largest to smallest, the horizontal spacing is 240, 80, 26.7, 26.7, 8.9, 8.9, 8.9, 2.96, 0.98, and 0.33 km. Since the mother domain is the one with the highest and poorest resolution, it is the one we start with and the one that is configured with the standard initial boundary conditions, which come from the NASA Ames General Circulation Model. The successive grids take the following conditions as initialization conditions.

Table 2. MRAMS parameterization values.

Ls	Season	sol	MSL_{elev}	$MRAMS_{elev}$	α	TI	τ
			MY32				
Ls 0°	spring equinox	350	−4500.205	−4502.680	0.242	341.446	0.151
Ls 90°	summer solstice	543	−4487.001	−4481.850	0.239	325.240	0.083
Ls 180°	autumnal equinox	722	−4457.023	−4450.690	0.233	316.563	0.146
Ls 270°	summer solstice	864	−4459.712	−4444.020	0.231	313.173	0.194
			MY36				
Ls 0°	spring equinox	3024	−4077.100	−4069.530	0.234	315.237	0.151
Ls 90°	summer solstice	3217	−4018.350	−4021.060	0.235	316.831	0.083
Ls 180°	autumnal equinox	3396	−3964.720	−3975.500	0.231	324.870	0.147
Ls 270°	summer solstice	3539	−3897.650	−3893.420	0.235	327.084	0.194

MRAMS parameterization values to simulate the Curiosity rover's position in years MY32 and MY36 (differentiated in shaded color), according to the solar longitude, Ls, of each equinox (Ls 0° and Ls 180°) and solstice (Ls 90° and 270°). The seasons corresponding to Ls are in the second column. For each solar longitude, the corresponding sol, on which a simulation has been performed from which the results of atmospheric pressure and temperatures discussed in Section 3.2 are obtained. For each sol, the rover elevation, $MRAMS_{elev}$ was entered into the model approximating as closely as possible the actual elevation, MSL_{elev}, for that sol. As well as the albedo, α; thermal inertia, TI; and atmospheric opacity, τ.

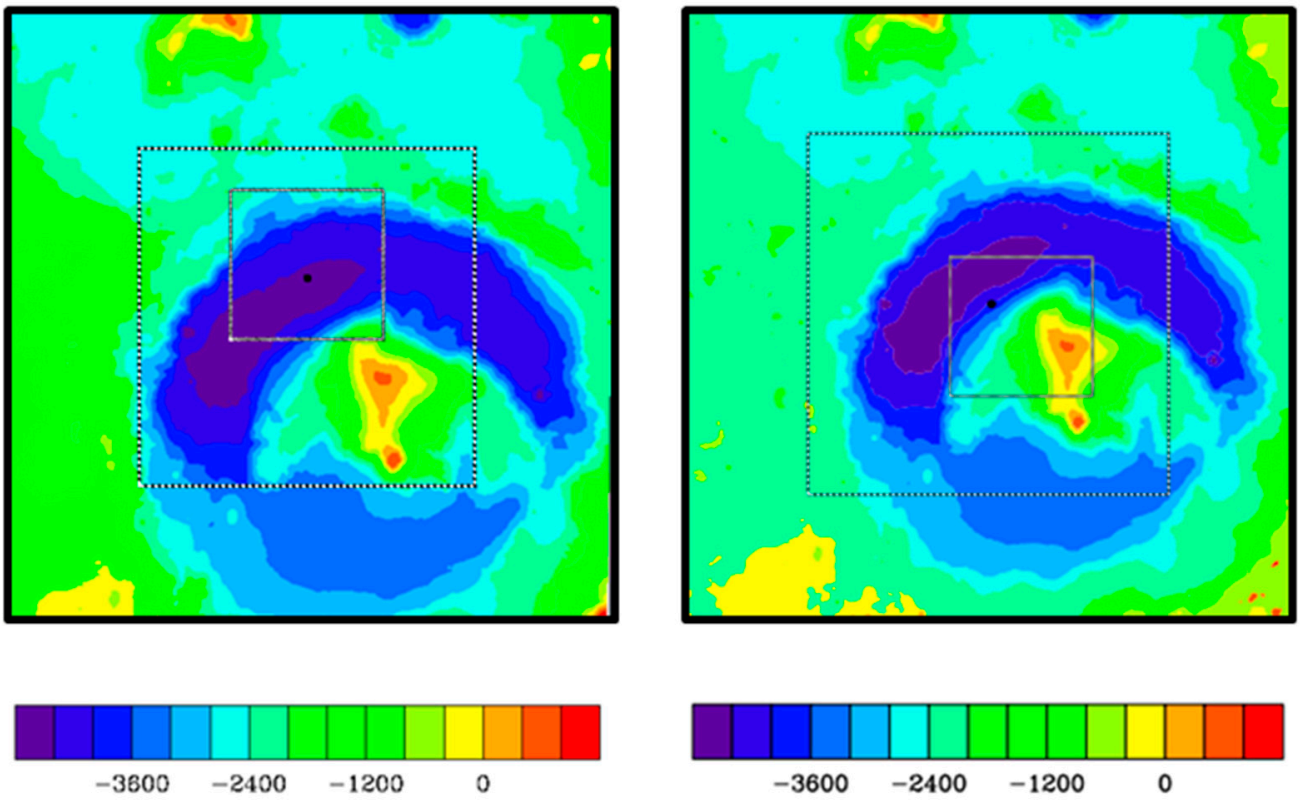


Figure 3. Topographic environment considered for the calculation of atmospheric pressure and temperatures at the location of the Curiosity rover in MY32 (image on the **left**) and in MY36 (image on the **right**). Both images show the last two nested grids of the total seven calculated. The white dot inside the smallest grid indicates the position of the rover. The color scale indicates the altitude of the terrain in meters.

The minimum height at which the model predicts atmospheric temperatures is 14.5 m above the ground, and, therefore, the closest to the 1.5 m at which the REMS sensors measure. It is also relevant that this model does not include clouds; the variations in albedo and thermal inertia are changed using the values in Table 2 [21]. Ideally, this first vertical level would be set to align with the height of the REMS sensors at around 1.5 m. However, achieving this is computationally impractical due to the non-hydrostatic nature of the model, where the integration time step is directly constrained by the thickness of the model layer. Reducing the layer thickness to approximately 1.5 m would require a mother domain time step of just fractions of a second, which would, in turn, increase the required simulation time by nearly two orders of magnitude [22].

3. Results from REMS Observations and MRAMS

This section presents the results for the interannual (Section 3.1) and daily (Section 3.2) time scales. This section, dedicated to the daily time scale, compares REMS and MRAMS.

3.1. Interannual Scale Results from REMS Observations

We report of 3967 sol observations performed by REMS from MY 31through part of MY37. We show the annual evolution of the atmospheric pressure, atmospheric temperature, surface skin brightness temperature, relative humidity (RH), and water vapor volume mixing ratio (VMR). We calculated the values presented using measurement sessions that lasted at least five minutes.

Figures 4 and 5 show the atmospheric pressure data, and the values shown correspond to the daily average of the readings of all the measurements for each sol. The range of

daily pressures usually oscillates, concerning the mean value, around 60 Pa, which will be addressed in the next section, but for the interannual scale analysis, we focus on average values, which is sufficient for this analysis. As expected, the surface pressure decreases as the rover ascends Mt. Sharp since the atmospheric mass per unit area decreases with increasing altitude [23]. Figure 4 shows the annual evolution of the mean pressure values versus solar longitudes. As expected, e.g., [24], the absolute maximum is detected between 240° < Ls < 270°, while the relative maximum is between 35° < Ls < 60°. The minimum is found at Ls 150° and near Ls 360°; a relative minimum is inferred [23]. The maximum measured pressure value detected was ~925 Pa, while the minimum was around ~700 Pa. Figure 5 shows the evolution of the atmospheric pressure as a function of the sols and the change in altitude as the rover ascends the slope of Mt. Sharp.

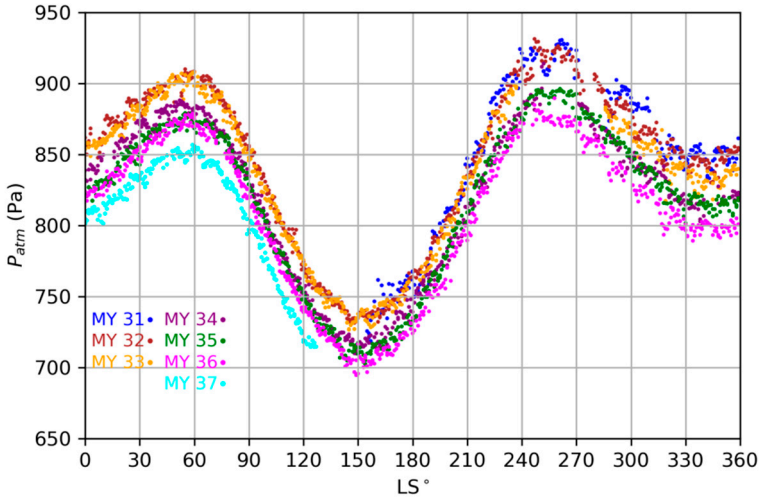


Figure 4. Seasonal evolution of daily mean atmospheric pressure (P_{atm}) during the first 3967 sols of the MSL mission. The color code is used to represent different Martian years.

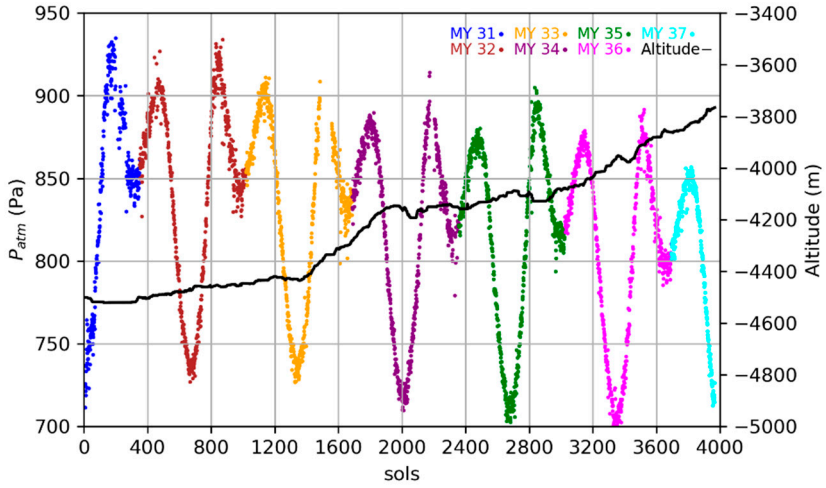


Figure 5. Seasonal evolution of daily mean atmospheric pressure during Curiosity's traverse and altitude changes during the first 3967 sols. The color code is used to represent different Martian years. The black line represents the altitude of the Curiosity rover.

The daily temperature variability is shown graphically in Figure 6. The average values per sol of the atmospheric temperatures result from first calculating the absolute maximum and the absolute minimum. These correspond to the local maximum and minimum of each sol. After, at the respective times when the maximum and minimum occur, a grouping of the values at a time difference of 15 min and the average of all of them is made. Finally,

the mean of each sol is calculated as the average between the maximum and minimum obtained, as explained above.

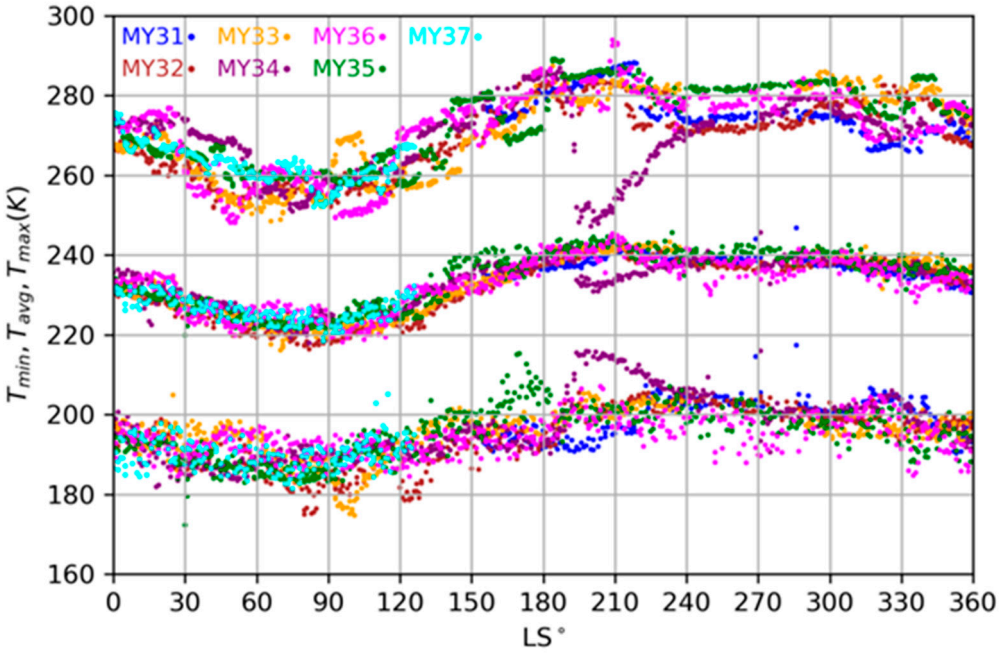


Figure 6. Interannual and seasonal evolution of daily maximum, central value, and minimum atmospheric temperature during the first 3967 sols of the MSL mission. The color code is used to represent different Martian years.

As shown in Figure 6, the minimum annual temperatures reach around Ls 90°, while the maximum temperatures peak around Ls 180°. Note the variation that occurred in MY34, which differs from the usual pattern of annual temperatures, caused by dust. In general, dust has an effect on the amount of solar energy that penetrates the lower layers of the atmosphere, reducing the amount of solar radiation that ultimately reaches the surface. However, dust enhances downwelling infrared radiation. As a result, increased dust levels lead to a reduction in surface solar heating and an increase in infrared radiation toward the ground, ultimately decreasing the diurnal temperature range at the surface.

The same behavior occurs with the surface brightness temperatures, presented similarly in Figure 7, although the variability between the minimum and maximum temperatures is more significant. Calculating the plotted values is analogous to the method applied to the atmospheric temperature.

In both cases, atmospheric and surface brightness temperatures showed a remarkable fluctuation in MY 34 between 185° < Ls < 210°, the great dust storm, especially prominent for the case of the maxima. This fluctuation manifests with an abrupt decrease in the maxima and a slight increase in the minima, leading to a decrease in the central values, e.g., [25]. The maximum temperature reached is ~275 K, occurring between 180° < Ls < 210°, and the minimum is ~185 K at Ls~90°.

Figures 8 and 9 show the results estimated for the daily maximum relative humidity and the corresponding value of the associated water volume mixing ratio (VMR), respectively. The high-quality hourly RH values were computed by selecting REMS-HS obtained with the latest recalibration parameters and taken only during the first four seconds of measurements after the REMS-HS was turned on after ~5 min of inactivity to avoid heating the sensor. These values include RH measurements taken during nominal and high-resolution interval modes (HRIMs). The HRIM measurement strategy consists of alternately switching the sensor on and off at intervals to minimize heating and is only used for selected

observations of ~one to two hours' duration [26]. Having made this selection, the daily maximum RH values were calculated, as shown in Figure 8, and occur between 04:00 and 06:00, e.g., [16,26–28].

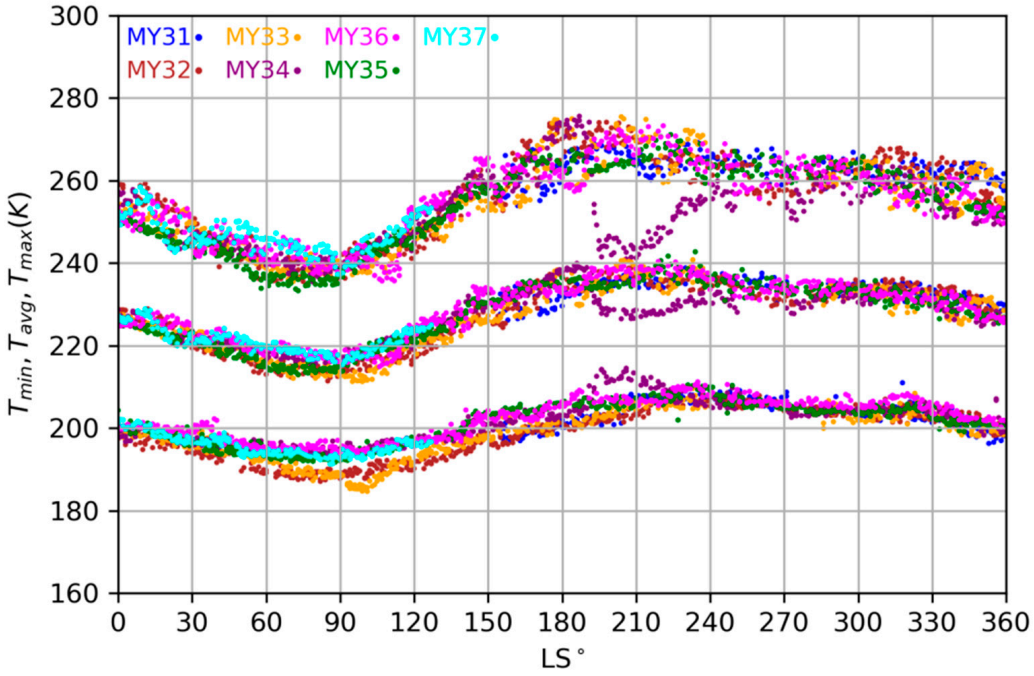


Figure 7. Interannual and seasonal evolution of daily maximum, central value, and minimum surface brightness temperature during the first 3967 sols of the MSL mission. Color code is used to represent different Martian years.

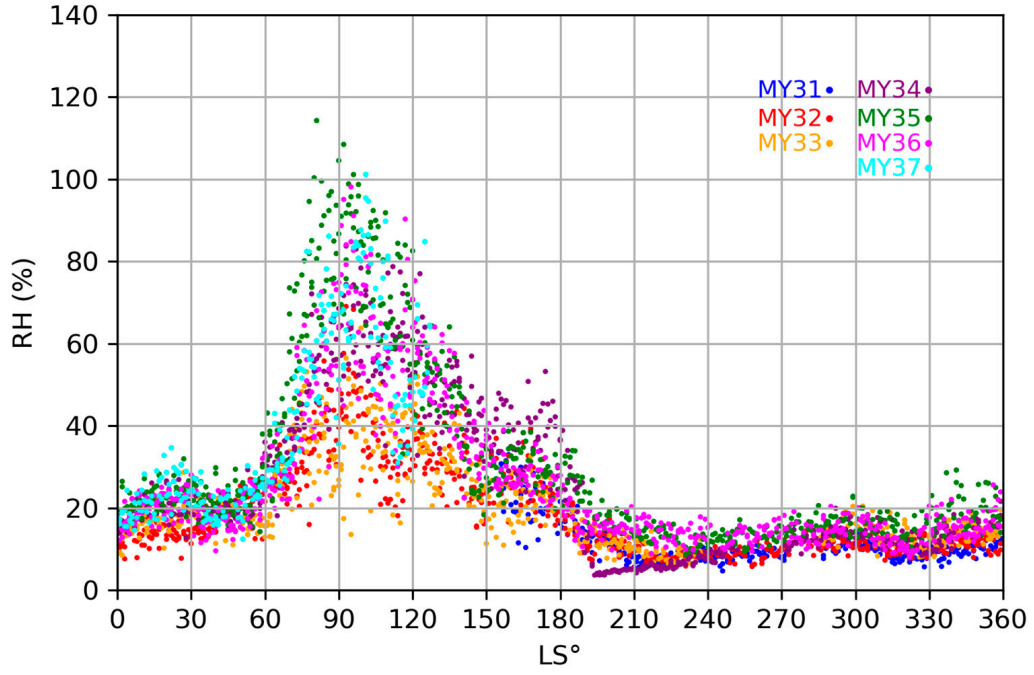


Figure 8. Interannual and seasonal evolution of the daily maximum relative humidity (RH) in the first 3967 sols between 04:00 and 06:00 LMST of the MSL mission. Color code is used to represent different Martian years.

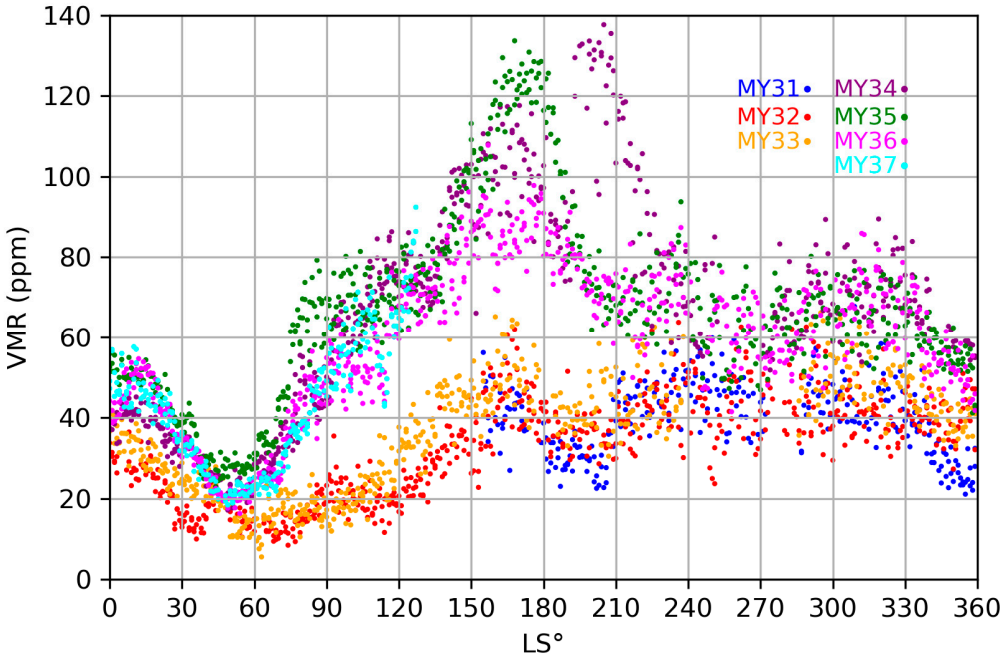


Figure 9. Interannual and seasonal evolution water VMR for the daily maximum relative humidity during the first 3967 sols of the MSL mission. Color code is used to represent different Martian years. The values used correspond to 4 and 6 LMST.

The VMR, in Figure 9, was estimated according to the expression VMR = RH·e_s(T)/P, where RH is the maximum daily relative humidity, e_s the saturation water vapor pressure above the ice, and P is the atmospheric pressure [26–28].

3.2. Comparisons of the Diurnal Cycle Between REMS and MRAMS at Two Locations

The atmospheric pressure and temperature results obtained from the REMS measurements and MRAMS simulations are presented together in Figures 10 and 11 for the solstices and equinoxes. These are used to compare the environment in which the Curiosity rover was located in MY32 and MY36 daily. These years have been chosen because in one, MY32, the rover was at the bottom of the crater, while in MY36, it was at an altitude of ~740 m above the landing site altitude on its ascent of Mt. Sharp, with sufficient data to, in each case, cover both years entirely (MY31 and MY37 could have been chosen but complete annual data were not available). Since MRAMS operates on a daily scale, the comparison has been performed for Ls 0°, 90°, 180°, and 270° to reflect the four main seasons of a year and also represent a Martian year. Although REMS sensors measure at 1.5 m and MRAMS simulates the measurement at 14.5 m, the comparison allows us to evaluate the predictive ability of MRAMS for near-surface atmospheric processes and to emphasize where the most considerable discrepancies between the model and measurements occur. For the experimental atmospheric pressure data, in Figure 10, and temperature data, in Figure 11, each plotted point corresponds to the average of the five-minute intervals of the five sols closest to the solar longitude of interest.

The differences in the pressure, in Figure 10, between the model and the measurements, are most prominent at the vernal equinox (Ls 90°) and at the summer solstice (Ls 270°). These discrepancies will be discussed in the following section.

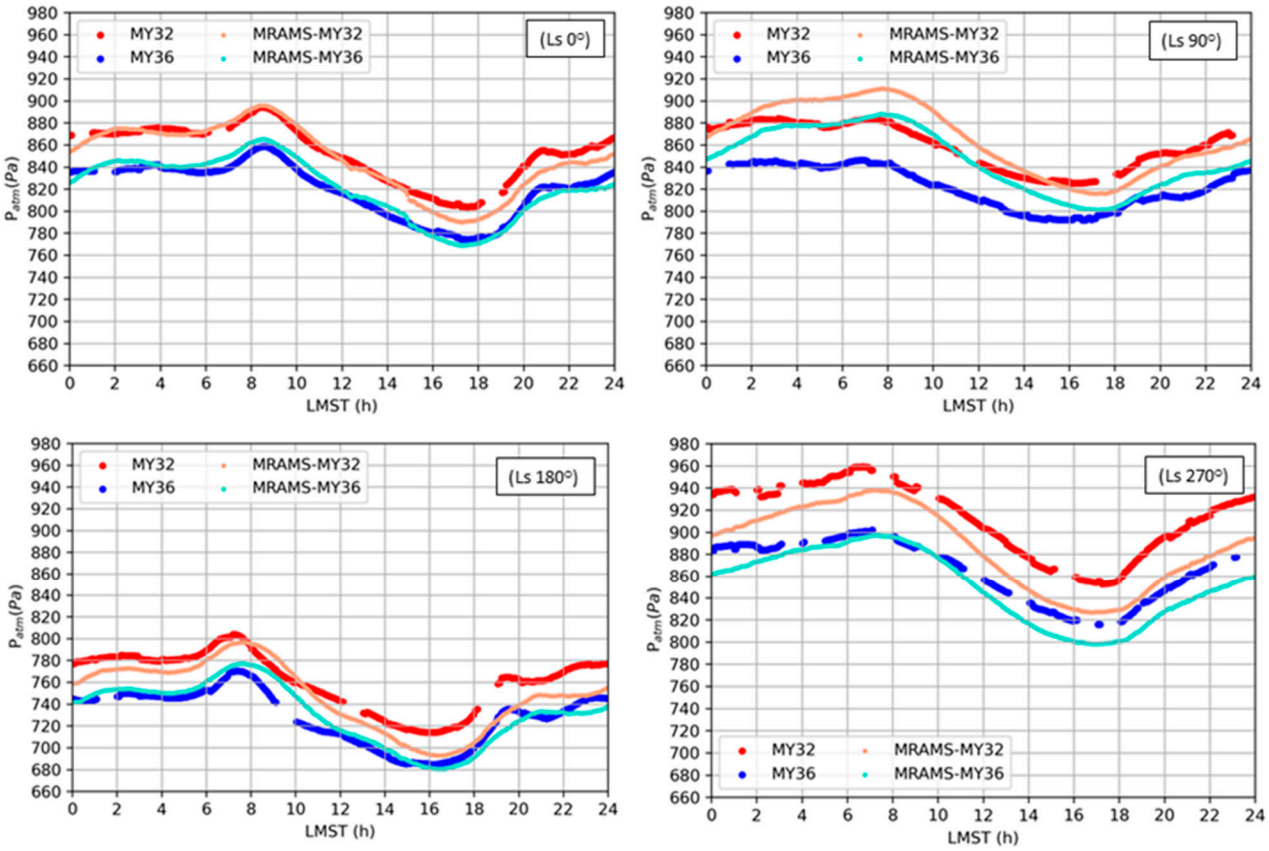


Figure 10. Daily scale of atmospheric pressure behavior in MY32 and MY36 in LMST. The sols of each year closest to the solstices (Ls 0° y Ls 270°) and equinoxes (Ls 90° y Ls 270°) are represented for REMS and MRAMS. The sols correspond to the classification in Table 2.

Regarding the atmospheric temperature, in Figure 11, the main difference between the MRAMS predictions and REMS measurements of the atmospheric temperature for all scenarios occurs again at the spring equinox and the winter solstice. Due to the model's output being derived from approximately 14 m above the REMS sensors, we anticipate that MRAMS temperatures at higher altitude from the ground will generally be lower than the observed values during the morning and early afternoon, with this discrepancy becoming more pronounced as the sol progresses. Conversely, in the late afternoon and overnight, MRAMS is expected to show higher temperatures. This behavior can be attributed to the steep afternoon superadiabatic lapse rate and a significant nocturnal inversion, e.g., [29,30]. Throughout the day, the discrepancies in the air temperature between the model and observations are largely influenced by convective processes. The notable rise in the air temperature during the evenings, coinciding with the onset of radiative cooling, along with the rapid fluctuations in the modeled night-time temperatures throughout the year (Figure 11), suggests the presence of nocturnal turbulence. This turbulence may be mechanically induced, causing warm air to descend and cold air to rise, particularly as the atmosphere stabilizes during the evening and night-time hours [31]. The predictions of the MRAMS reflect this exceptionally well. However, while the discrepancies will be analyzed in detail in the next section, the most significant differences occur at the spring equinox (Ls 180°), where the correlation between the instrument and the model is weaker, similar to what was observed in the case of pressure (Figure 10).

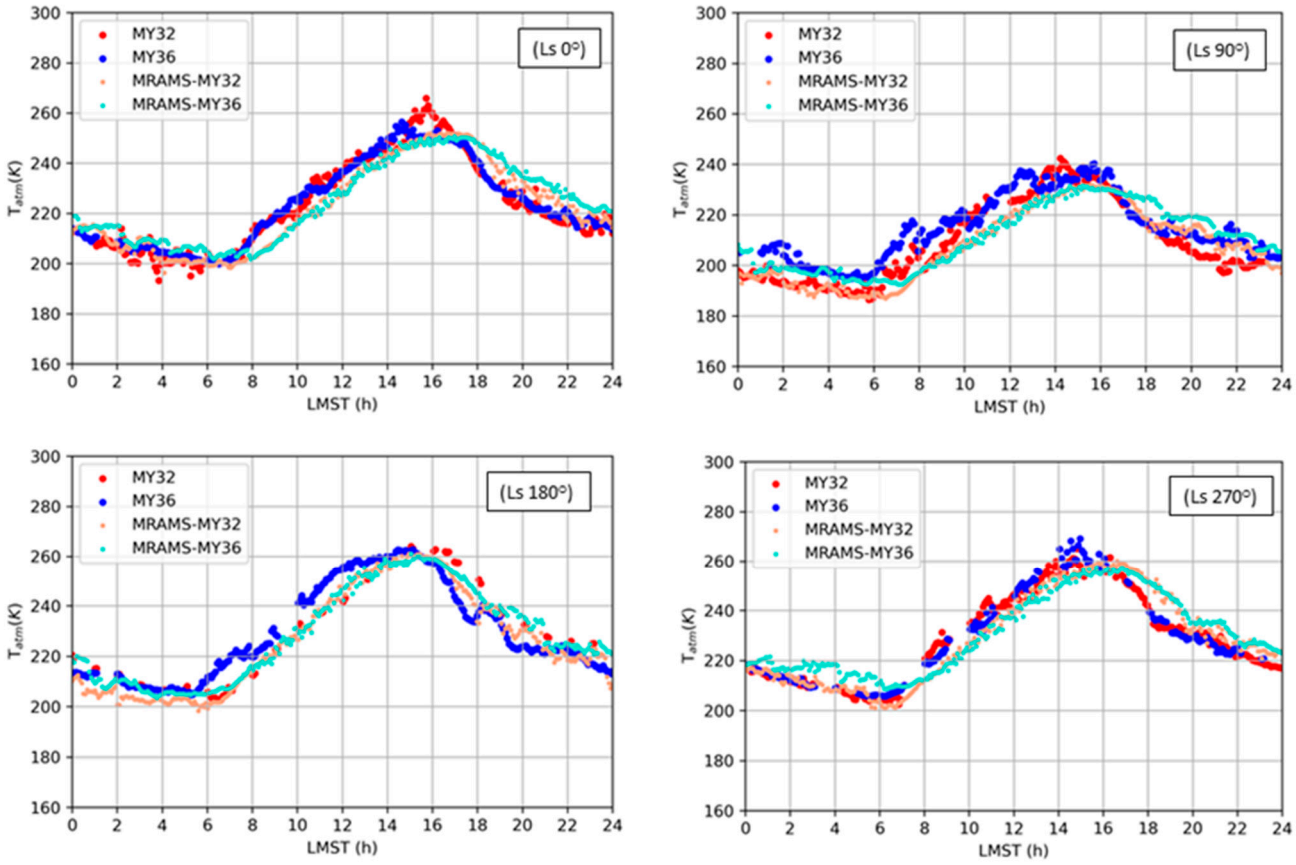


Figure 11. Daily scale of atmospheric temperature behavior in MY32 and MY36 in LMST. The sols of each year closest to the solstices (Ls 0° and Ls 270°) and equinoxes (Ls 90° and Ls 270°) are represented for REMS at 1.5 m and MRAMS at 14.5 m. The sols correspond to the classification in Table 2.

4. Analysis and Discussion

4.1. Interannual Scale

As expected, the pressure decreases as the rover ascends Mt. Sharp. Figure 5 shows that the sharpest drop is between the end of MY33 and the beginning of MY34, when the rover started to ascend the slope of the mountain. The pressure maxima and minima coincide with periods of atmospheric CO_2 sublimation and freezing, e.g., [32,33]. The pressure step between MY33 and MY34 results in a difference between the maxima and the minima of each year of ~25 Pa, as can be inferred from Figure 5, to an ascent at a height of ~350 m. Table A1 (Appendix A) provides a register of the maximum and minimum pressure values associated with the elevation and altitude of the rover, as well as the orbital position of the planet for the years studied. These values correspond to the variations in the Martian day and are not based on the mean of the day shown in Figures 4 and 5.

Figure 12 shows the results of pressure normalization by eliminating the contribution to the pressure decrease due to the effect of ascent. This correction allows us to focus on the dynamic effects (variations in the composition of the dust column, weather fronts either warm or cold, wind effects capable of redistributing the air masses and thus affecting pressure). Ref [23] used rover data to calculate this correction. Here, data from the Mars Climate Database model [34,35] have been used to calculate adjustment factors for the pressures of each year, accounting for rover elevation. These factors have been used to multiply the measured pressures in Figures 4 and 5 to produce the graphical results in Figure 12.

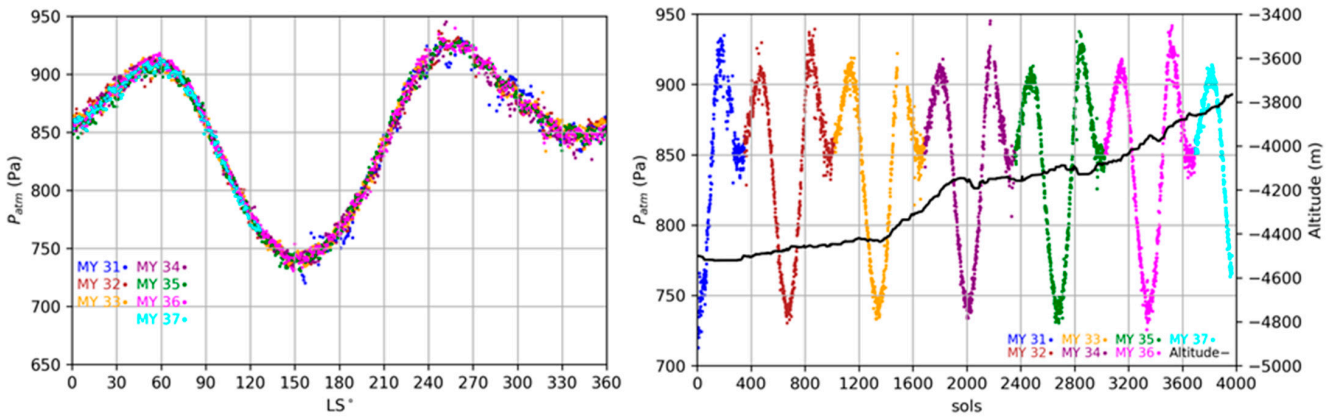
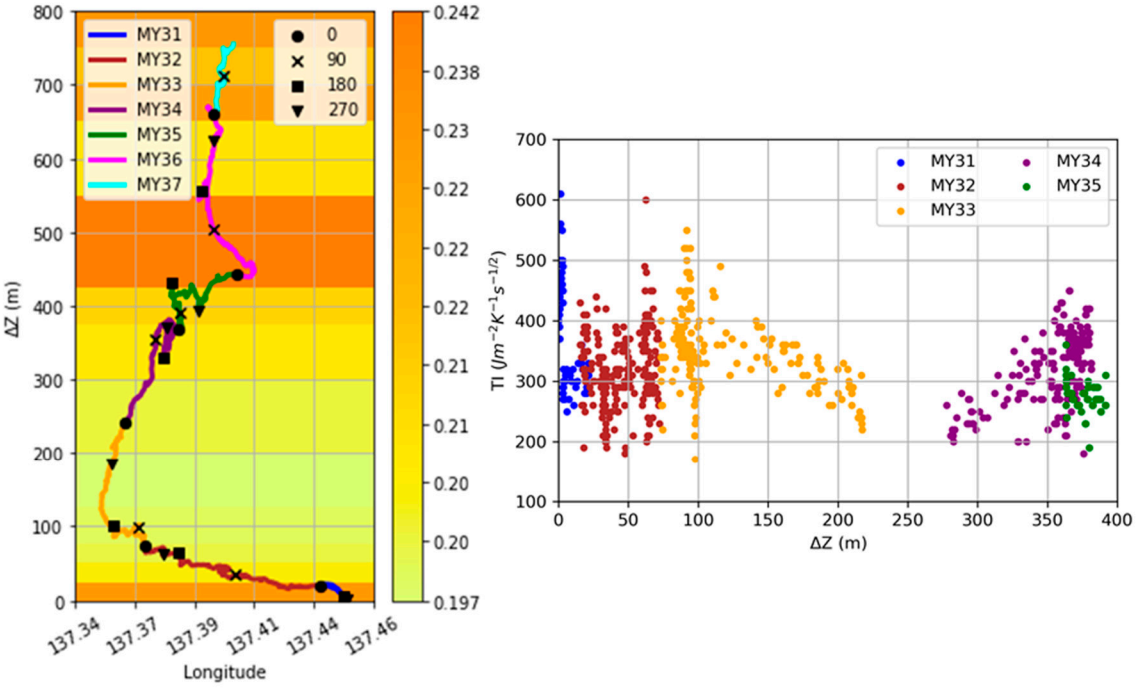


Figure 12. Normalization of the pressure values shown in Figures 4 and 5 to the landing altitude of the rover, to remove the effects of the change in elevation of the rover along its trajectory. (**left**) Atmospheric pressure, P, versus solar longitude, Ls. (**right**) Atmospheric pressure, P, and altitude versus the sols. The rover trajectory is represented by the black line.

As for the atmospheric temperatures, shown in Figure 6, and surface brightness temperatures, shown in Figure 7, there is a remarkable similarity in how their behavior evolves annually. Tables A2 and A3 (Appendix A) provide a record of the maximum and minimum values of the atmospheric and surface brightness temperatures, respectively, associated with the elevation and altitude of the rover as well as the orbital position of the planet for the years studied. It should be noted that the fluctuation in both temperatures was detected in MY34, around Ls~210°, which corresponds to the global dust storm (GDS) already analyzed by [36–38], among others. As can be seen, the dust effect causes the maximum temperatures to decrease and the minimum temperatures to increase. Dust is an effective absorber of solar radiation. Solar radiation contributes to lowering the daytime temperature and increasing the night-time temperature by not allowing the radiation emitted by the ground, which was previously heated by solar radiation, to pass through. Another remarkable fluctuation is the one found in MY33 at 90° < Ls < 100°, the behavior of which is the inverse of that produced by the GDS, with the maxima increasing and the minima decreasing more than their respective oscillation ranges. This phenomenon coincides with the rover crossing an area of active dunes, Nabim Dune [39,40]. This fluctuation could be due to albedo and thermal inertia variations, so the analysis performed here of both properties allows us to evaluate how much they influence this fluctuation. For albedo, measurements from the OMEGA instrument onboard the Mars Express orbiter and TES aboard the Mars Global Surveyor (MGS) have been used for thermal inertia calculation. The spatial resolution for OMEGA varies from 300 m to 4 km [41,42], and for TES, it is 3 km [43].

The albedo analyzed is presented in Figure 13a, highlighting for each year the Ls of most significant interest in this study. It was found that the MY33 event coincides with the lowest albedo value of the entire mission (compatible with the observed diurnal ground brightness temperature data), Figure 13a. Then, for the period in which the fluctuation is found, no albedo change could cause the detected phenomenon. For example, the value is the same for Ls~90° and Ls~100°, at 0.199.



(**a**) (**b**)

Figure 13. (**a**) Elevation change (ΔZ) together with the albedo change indicated by the color scale. The albedo data are taken from the OMEGA instrument onboard the Mars Express orbiter. The length of the rover along its trajectory is indicated and divided into color-coded sections corresponding to the Martian year in which it traveled. Also, different signs are marked in each year where the Ls values of 0°, 90°, 180°, and 270° are given. (**b**) Thermal inertia (TI) versus elevation change. The thermal inertia data are from the TES instrument on the MGS orbiter, and at the time of this investigation, there are not enough sols available to cover up to MY37, as is the case with the REMS measurements. However, they do allow us to claim that the tendency of the thermal inertia is to vary in each year within a constant range between 200 and 500 regardless of whether the elevation change increases in each year.

However, this lack of albedo variation could be due to the spatial resolution of OMEGA being too low compared to the distance traveled by the rover between Ls 90° and Ls 100°. In other words, during the path traveled by the rover in this period, OMEGA has not changed pixels. Thus, what is happening is that the OMEGA measurement is an average pixel value. The analysis of the available TI data for the year MY33 has been carried out, and the graph in Figure 13b is shown. For example, the values for the event period of MY33 (see Figure 7) are for Ls~90° and 180°, and for Ls~100°, the value decreased to 170. So, although TES has a resolution of 3 km and the rover in this period does not have time to travel this distance in which the spatial resolution of the instrument has changed, a variation in TI is found, which is also compatible with the temperature evolution given in the results section. Likewise, the low values found here, both for TI and albedo, also coincide with the dune area in which the rover was located and with the research of [40], from which it is inferred that the higher dust density is affecting it.

To examine how the change in altitude influences the atmospheric temperature, the potential temperature of the daily maximum, mean, and minimum (night temperatures) has been calculated. It is illustrated in Figure 14a, Figure 14b, and Figure 14c, respectively. In all cases, it is observed that the temperature increases as one ascends; the increase is more noticeable in the minimum values than in the case of the mean and maximum, as can be seen in Figure 14c.

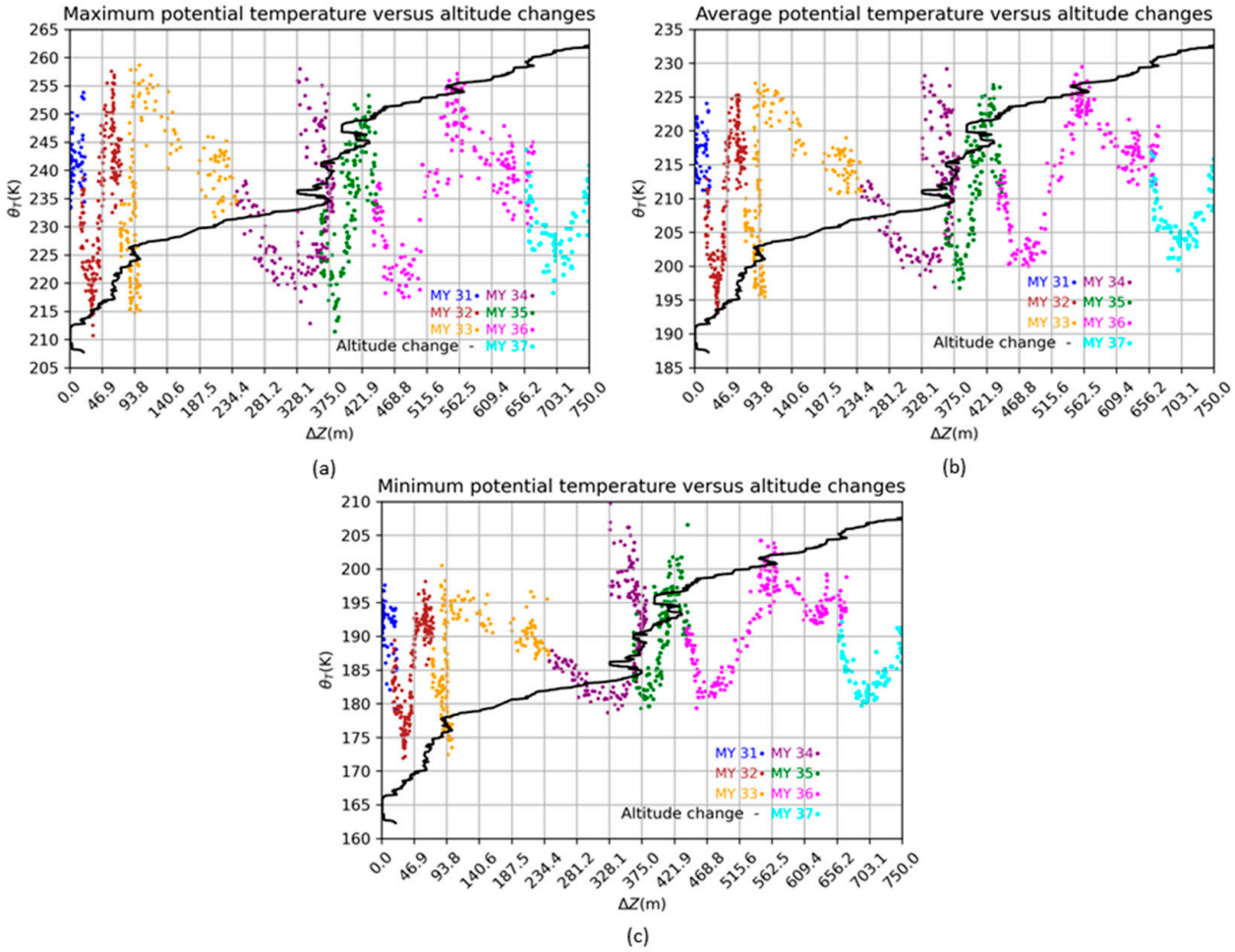
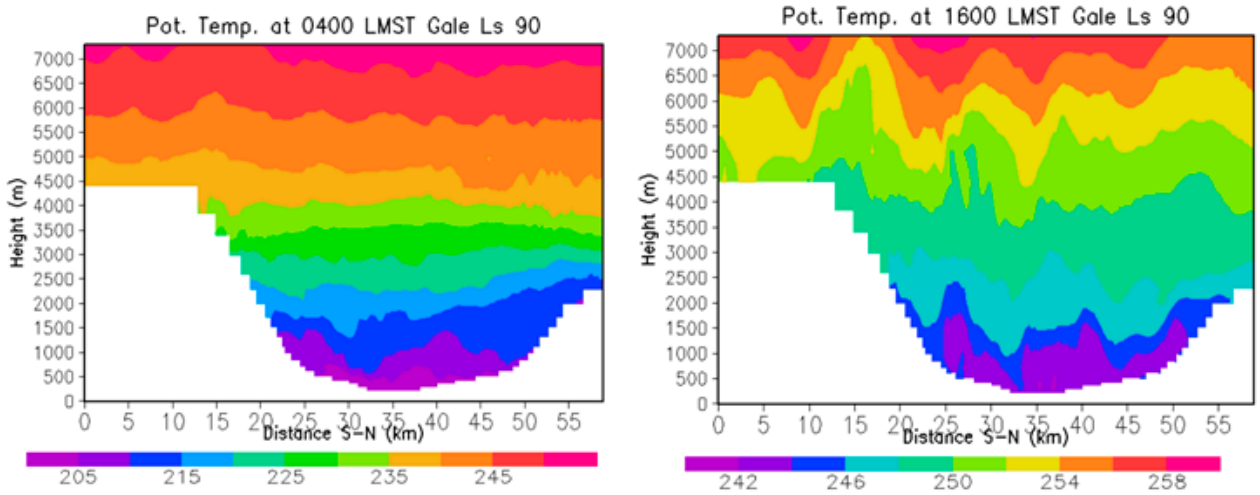


Figure 14. Potential temperature (ΘT) of daily maximum (**a**), mean (**b**), and minimum (**c**) versus change in elevation (ΔZ). Each color indicates the corresponding section for each year. The solid black line represents the trajectory of the Curiosity rover.

As the rover ascends, the minimum value of the night temperatures increase. This thermal increase suggests that the rover, as it reaches higher latitudes, leaves an area (the crater floor), where cold air masses accumulate during the night. The difference in the minimum night temperatures reached in MY33 and MY34 differed by ~5 K. From the second half of MY34 onwards, the minimum night-time temperatures (Figure 14c) remain nearly constant. This sudden transition is consistent with the rover climbing above a cold pool of air to enter into the thermal belt altitude of Gale crater, where night-time minima are constant because the rover is more exposed to mixing with the free atmosphere and outside hypothetical accumulation of cold air masses that drain at night into lower altitudes. This would agree with the results simulated with MRAMS (Figure 15) for Ls 90° at the minimum temperatures at 04:00 h and the maximum at 16:00 h shown in Figure 15.

Among the findings shown here (Figure 14) is that the 5 K rise between MY33 and MY34 is found at minimum potential temperatures (night time) above ~290 m and remains stable. However, at maximum potential temperatures, this 5 K rise occurs between MY36 and MY37 and at ~328 m, which is a slightly higher elevation rise. Both findings are consistent with the MRAMS simulations shown in Figure 15.



(**a**) (**b**)

Figure 15. Vertical cross-section (south to north) of potential temperature from MRAMS for LS 90 at (**a**) 04:00 and (**b**) 16:00 LMST. Mt. Sharp is the hill on the **left**. The north crater rim is the hill on the **right**.

Figure 15 shows the potential temperature obtained from the MRAMS simulation. Comparing the figures in that panel, it can be seen that the simulated atmosphere is much more stratified in the night period, particularly at 04:00 (Figure 15a) than in the daytime, at 16:00 h (Figure 15b). It can also be noted that the colder air accumulates during the night at the bottom of the crater, while during the day, there is a more effective mixing of air masses. Therefore, it is necessary to reach a higher altitude to observe the same temperature changes as during the night.

To see the joint impact of the seasonal cycle together with the change in altitude and location, Figure 16 presents the correlation between the change in elevation and the respective solar longitudes for the daily minimum atmospheric temperature. Looking at Figure 16, we deduce that the atmospheric minimum temperatures reach the minimum values in the range of $80° \lessapprox Ls \lessapprox 110°$.

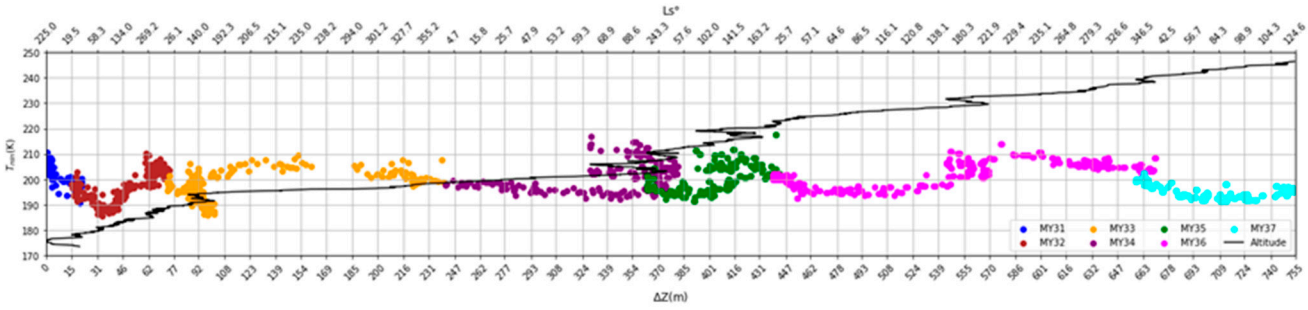


Figure 16. Evolution of daily minimum atmospheric temperature versus elevation changes (ΔZ) along the rover trajectory (black line). Although the general trend of the rover trajectory is upward, it rises and falls along its path, which can be seen in the irregularities along the trajectory. In addition, the upper horizontal axis shows the solar longitude (Ls) corresponding to the elevation depicted, which allows the reader to place the rover in the annual season.

Despite the changes in location and pressure, the minimum atmospheric temperature values occur in all years around Ls~90°, as seen in Figure 6. At this solar longitude of the planet, the seasonal formation of water ice clouds occurs [44]. As Mars approaches its most significant distance from the Sun, at aphelion, i.e., around solar longitude Ls~71°, the planet's atmosphere cools, and there is a decrease in dust lifting along with a marked

increase in cloud formation and density [45,46]. As Mars approaches the northern hemisphere autumnal equinox at Ls = 180°, the atmosphere begins to warm, and more vigorous dust lifting resumes, peaking at perihelion, Ls = 270°, the dust season. At the same time, cloud formation decreases [16]. The process repeats annually and gives rise to the Aphelion Cloud Belt (ACB) phenomenon. Moreover, during Ls~90°, the suspended water vapor is higher, which would favor the increase in cloud density, and that could be the reason for the higher RH maxima in this period, as shown in Figure 8, which is in agreement with the literature [27,45]. Also, this is around the northern summer, when the polar cap there is exposed by losing seasonal CO_2 ice cover, which increases the vapor release to the atmosphere. The results shown here are consistent with possible strong water condensation in this seasonal period and agree with studies based on orbiter measurements that maintain the existence of a saturation cycle with humidity increases occurring in the same periods [46,47].

While finding a repeated annual cycle, we also find that these properties varied significantly as the rover ascended Mt. Sharp. The abrupt increase in this year-to-year maximum observed in these results is also attributed to the rover having reached an elevation where conditions are influenced not only by the stable inversion layer that develops on the floor of Gale Crater at night but also by the penetration of the overlying atmosphere. The joint analysis of Figures 8 and 9 shows that the seasonal evolution of the maximum RH and VMR are not directly proportional [28]. An important part of the fluctuations in the maximum VMR is thought to be due to the uncertainty of the VMR values introduced by the large sampling gaps that often misses the actual maximum and not to the actual variations in the maximum VMR [26]. Yet, in a statistical sense, there should be enough sols that do capture the true maximum and eliminate a non-existent trend with the altitude.

Additionally, it is remarkable that, by analyzing the RH together with the change in elevation, as shown in Figure 17a, it is detected that the range in which it varies increases, particularly from MY34 onwards. Between MY31 and MY33, no year exceeds 70%, while MY34 and MY37 both exceed 80%, despite both years displaying warmer night-time temperatures. This is consistent with having reached higher altitudes, where the rover is more exposed to a moisture-free atmosphere. Analyzing the variation in VMR as a function of elevation change, shown in Figure 17b, the number of water molecules in suspension also increases with increasing elevation. It is observed that up to MY33, no year exceeds 60 ppm, and after that, all reach 80 ppm. The maximum VMR ranges between 120 and 140 ppm and occurs in MY34 and MY35. Also, in these years, the maximum RH values reached saturation. Saturation on Mars occurs below 10 km during the boreal spring/summer [27]. Condensation produced by this saturation could occur at low latitudes due to the freezing nights on Mars, e.g., [26,48,49]. Thus, the results indicate that the rover has passed through an area where the temperature conditions are optimal to reach saturation. In addition, it is known that on Mars, in the northern polar cap, the seasonal cap sublimates almost completely during spring and early summer, exposing all or most of the underlying residual water ice layer, e.g., [44,50]. The water ice then sublimates, the water vapor content of the atmosphere increases, and winds carry it away [18,19,45].

Figures 9 and 10 show that the season where the VMR reaches its maximum does not coincide with RH's due to the effect of temperatures in increasing the RH exponentially as temperatures cool down. It is possible that winds forced the hot air masses to sink to the bottom of the crater, preventing them from ascending by buoyancy. This would result in complete air circulation of the crater annually, which impacts suspended molecules such as water molecules. This process would then justify some of the behavior of the VMR, especially from Ls~180° to Ls~270°. Other reasons for this are that this period includes the

strongest winds [51] and that higher altitudes within the crater are more exposed to more suspended water molecules carried by the sublimation of the south polar cap [30,44].

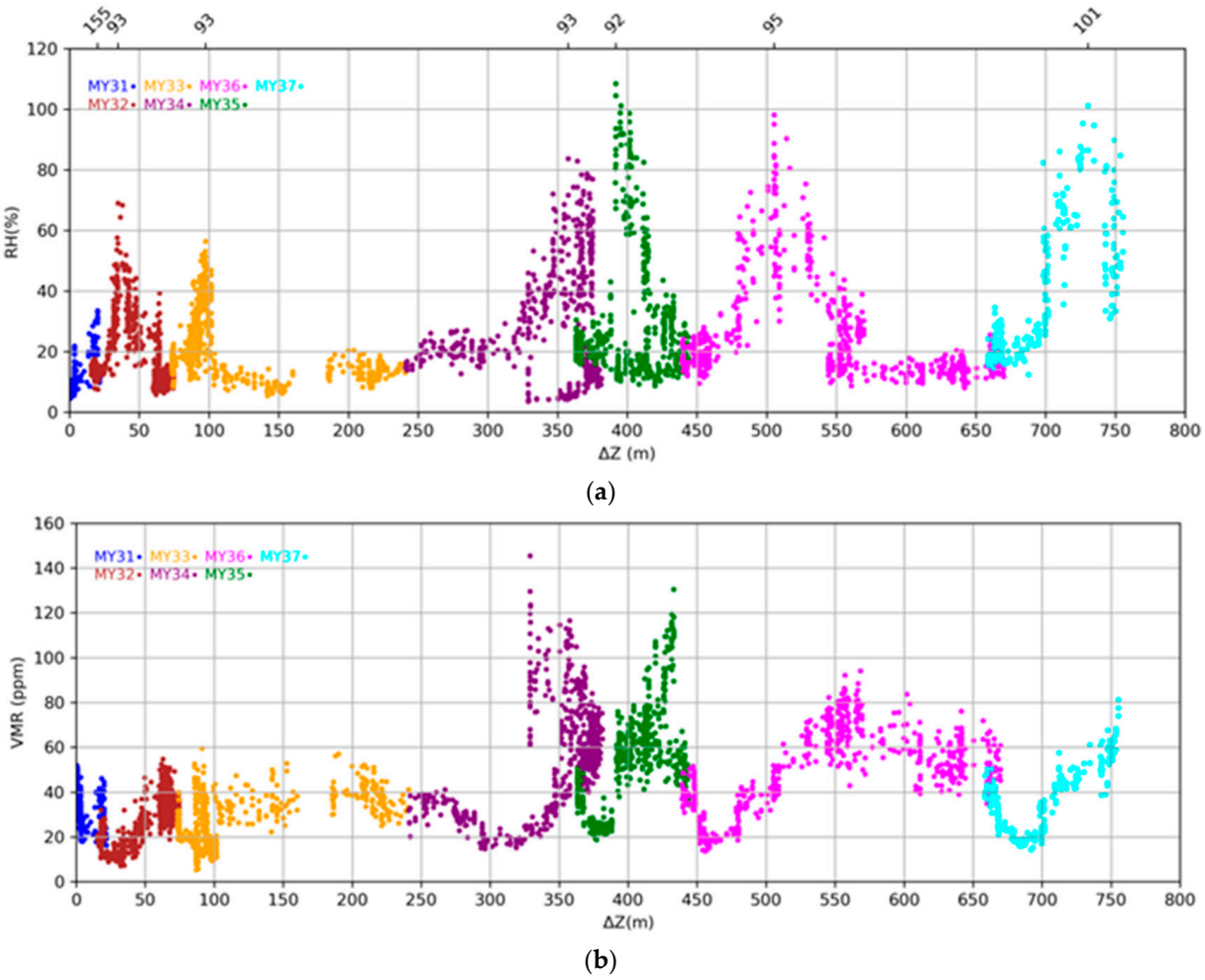


Figure 17. (**a**) Relative humidity (RH) versus change in elevation (ΔZ). The local time when the relative humidity values are relevant is 4 to 6 LMST. The solar longitude at which the maxima occur for each year has been searched for and indicated on the upper axis. All maxima occur between 90° < Ls < 160°. The years are distinguished by color. (**b**) Water molecule volume mixing (VMR) versus elevation change (ΔZ). Years are distinguished by colors. Although the increases in VMR annually coincide with those in RH, the maximum peaks in each year are not directly proportional between the two magnitudes.

On the other hand, the TI, shown in Figure 13a, and the albedo, shown in Figure 13b, support the reason that could be responsible for the increase in temperatures and variations in the VMR and RH along the rover's trajectory. Nevertheless, if so, a change in the albedo and TI would have to be found in the periods and locations where the change in the RH, VMR, and temperatures is detected. However, no linkage is found when comparing the evolution of these magnitudes with the albedo and TI presented. The temperatures have continued to increase gradually as the location has changed, although there are zones in which the albedo shows remarkable variation. For example, the albedo increases from MY35 to MY36 and then decreases again in MY37, while the thermal increase did not cease in any section. The same applies to TI, which oscillates between 200 and 500, irrespective of the location.

4.2. Mesoscale in MY32 and MY36: Comparisons Between REMS and MRAMS

It should be noted that the MRAMS uses dust values considered from Thermal Emission Spectrometer (TES) measurements from orbit. Thus, the tau value that MRAMS gives, 9 μm, leads to the assumption of a factor of 2 to convert to 880 nm visible opacity like those given by Mark Lemmon [52], which are based on the Curiosity's optical depth observations. Therefore, from the comparison between the MRAMS and Lemmon dust values, the possible difference, especially at Ls 180° and Ls 270°, could be due, in part, to the inclusion of total extinction (i.e., scattering) and the possible presence of water ice clouds in the Curiosity's observations, whereas the MRAMS dust values (measured by TES) only measure absorption.

The REMS and MRAMS results for both pressures and temperatures show a substantial variation between day and night in Gale Crater's environment. The discrepancies have been estimated by calculating the root mean square value for both pressures and temperatures, using Equation (1), between the measured and simulated data. Additionally, since a time lag was observed in the case of the pressures, the time lag value has been adjusted to minimize the root mean square error, as shown in Equation (2).

$$E = \sqrt{\sum_{F_{REMS}(t=0)}^{24} \frac{(F_{REMS}(t) - F_{MRAMS}(t))^2}{\sum N}} \quad (1)$$

$$E_s = \sqrt{\sum_{F_{REMS}(t=0)}^{24} \frac{(F_{REMS}(t) - F_{MRAMS}(t-s))^2}{\sum N}} \quad (2)$$

where E is the error between REMS and MRAMS and s is the time lag that minimizes E. Thus, E_s is the error minimized by the s that minimizes it the most.

The maximum difference between the maximum and minimum pressures (Figure 10) occurs at the vernal equinox, Ls 90°, and at the winter solstice, Ls 270°. Also, regardless of location, it is at Ls 180° and Ls 270° where the most extensive and smallest ranges of pressure oscillation occur, respectively. Ls 90° and Ls 270° show the most significant discrepancy between the REMS and MRAMS. In the Ls 90° period, there is an increase in the amount of water ice clouds, the formation of which is driven by the initiation of the sublimation of the north polar cap and the release of vapor from the regolith [30,44,45]. As for the poor correlation at Ls 270°, this may be due to the impact of obtaining the proper dust amount and vertical distribution in the MRAMS configuration. In this case, however, the cause is mainly attributed to the lack of wind considerations, and, in particular, the increase in the Hadley cell winds, which increase during this period [53,54], causing more turbulence. In turn, this turbulence is favored by the temperature increase in the southern hemisphere, due to the summer here during this period, which is consistent with research [46]. Also, the absence of clouds for this season in the model, may affect results.

Regarding the atmospheric pressure, the MRAMS approximates the qualitative behavior quite well. However, the ranges of values between which the pressure oscillates in the MRAMS simulations differ significantly from those recorded by the REMS. There is good agreement between the MRAMS and REMS regarding the atmospheric temperatures.

The measured atmospheric temperature or pressure is F_{REMS} (t), and the simulated values are F_{MRAMS}(t). The number of samples of total pressures or temperatures is N. According to the quantitative study of the errors made, the Ls 270° epoch has the highest pressure error, with 29.042 Pa in MY32 and 15.885 Pa in MY33, and with a time lag of 25 min in both years. The next epoch with the most considerable discrepancy, Ls 90°, has a discrepancy of 18.761 Pa in MY32 and 15.132 Pa in MY33, with a time lag of 80 min and 90 min, respectively. It is worth noting that during the night hours, between 18:00 and 00:00

LMST, the simulated temperature results are warmer than the actual measurements, while during the rest of the day, the opposite is true. This is consistent and could be related to the steep vertical lapse rates near the surface, negative at night and positive in the daytime, caused by the fact that the MRAMS calculates at 14.5 m and the REMS measures at 1.5 m.

Regarding the atmospheric temperatures, Ls 90°, during the Aphelion Cloud Belt (ACB) season, has the most significant estimated error. This epoch has a discrepancy of 6.169 K in MY32 and 8.706 K in MY33. The case of Ls 270°, during some of the highest opacities reported for the dust season, has a discrepancy of 5.958 K in MY32 and 7.339 K in MY33. Despite the discrepancies described, in general, and especially for the atmospheric temperatures, the MRAMS and REMS have sufficiently good overlap to consider that the model recreates the behavior of the atmospheric pressure and temperature in the environment of Gale Crater.

Comparing the two locations studied on a daily scale (MY32 and MY36) with the MRAMS and REMS (see Figures 10 and 11), the time range in which the atmospheric pressure maxima and minima occur is equally affected by the annual season for both locations. Daily maxima occur between 8:00 and 10:00 LMST at the spring equinox, Ls 0°, and the summer solstice, Ls 90°, and the minima occur between 16:00 and 18:00 LMST at the autumn equinox, Ls 180°, and the winter solstice, Ls 270°. Temperatures do not undergo this seasonal variation and maintain a maximum between 15:30 and 16:30 LMST throughout the year and the minimum between 5:00 and 7:00 LMST. In general, it can be said that in all cases, when the pressure decreases, the temperature increases in the time window, and when the pressure decreases, the temperature increases. This is due to the daily solar forcing that causes the atmosphere to expand upwards during daylight hours. The expansion thus produced at levels above the crater expands laterally to equalize the pressure around it. The air leaving the crater reduces the atmospheric pressure felt at the surface below the bulge. During the night, the opposite happens: the atmosphere compresses, and the surface pressure increases. This phenomenon, called thermal tide, e.g., [55–57], has been characterized here at both locations (with both the REMS and MRAMS). It depends on the time the atmosphere takes to respond to solar radiation and topography, among other factors. From the results obtained, location MY32 shows a more significant variation in pressure amplitudes between day and night than MY36 does. This is consistent with the predictions from the effects of the lateral hydrostatic adjustment mechanism, described by [58], changing with altitude.

5. Conclusions

Based on the REMS meteorological observations of the Curiosity's environments for 3967 sols, Gale Crater's complex meteorology combines the sum of the effects of air circulations at different scales. The interannual (global) and daily (local) scales have been studied here and compared to MRAMS model runs.

Among the meteorological changes found and analyzed with the REMS measurements, we highlight the progressive increase in the minimum atmospheric temperature as the rover reaches higher latitudes. The most significant rise in night-time temperatures occurs between the second half of MY33 and the beginning of MY34. This sudden change from low to higher minimum temperatures is characteristic of an accumulation of cold air masses; a 'cold air pool' formed by thermal drainage flows down the slopes of Gale Crater. The seasonal comparison with the MRAMS found that the seasonal period around Ls 90° stands out for being the one in which the atmospheric properties analyzed show the greatest discrepancies.

Having studied the physical quantities that could be affecting the temperature changes from one year to the next and finding that these quantities remain constant, even if the tem-

perature changes, we could say that the leading cause of the increase in temperatures along the rover's trajectory is the increase in elevation change. Furthermore, it has been found that this increase in temperature is more significant at its minimum (night-time temperatures).

The results presented here, obtained from surface measurements at the REMS meteorological station, support the existence of an atmospheric cycle near saturation, with a maximum RH around Ls 90° and an annual increase in the water VMR between Ls 100° and 270°. A comparison with other studies that have used satellite measurements shows that these results agree. In addition, this study shows that the topography conditions this atmospheric saturation since it favors the accumulation of cold air masses, which could be influencing it. In addition, the accumulation is favored in places of low altitude and limited by the slopes of the crater and Mt. Sharp, where the temperature is lower. The analysis of the increase in the VMR shows an increase at higher altitudes that is consistent with the vehicle being exposed to the free atmosphere and is thus more influenced by the mixing with air driven by the Hadley cell, which carries higher water molecules between both polar caps.

Once corrected for elevation changes in the model for the two locations where it is based (MY32 and MY36), and for each seasonal scenario studied, it is observed that the MRAMS results are above those of the REMS, with a difference of up to ~10 K between 18:00 and 00:00 LMST. The best coincidence between the model and measurements are found for the atmospheric temperatures. The worst correlation, in general, for both pressures and temperatures, is found at Ls 90°, where the MRAMS does not include the effects of clouds, and Ls 270°, where the vertical distribution of dust may be playing a role. Nevertheless, the lack of a better agreement of the model with reality is mainly found in the configured levels: 14.5 m vs. 1.5 m for the REMS. Also, the absence of clouds in the model parameterization seems to be favoring discrepancies. So, it can be stated that, for the most part, the MRAMS interprets the behavior of atmospheric pressure and temperature similarly to that measured by the REMS.

Author Contributions: Conceptualization and methodology, M.R.; REMS and MRAMS data processing to achieve results, M.R.; MRAMS data extraction, J.P.-G.; writing—revising and editing, M.R., E.S.-M., and J.A.R.-M.; revision, M.d.l.T.-J., J.P.-G., and S.C.R.R. All authors have read and agreed to the published version of the manuscript.

Funding: This research was funded by the Spanish Ministry of Economy and Competitiveness, through the projects No. ESP2006-27267, ESP2007-65862, AYA2011-25720, ESP2014-54256-C4-1-R, and AYA2015-65041-P; Ministry of Science, Innovation and Universities, projects No. ESP2016-79612-C3-1-R, ESP2016-80320-C2-1-R, RTI2018-098728-B-C31, MDM-2017-0737, and PID2021-126719OB-C41; Instituto Nacional de Técnica Aeroespacial; Ministry of Science and Innovation's Centre for the Development of Industrial Technology.

Data Availability Statement: The measurements from the REMS weather stations that have been analyzed for this research are available on the NASA server: https://atmos.nmsu.edu/PDS/data/mslrem_1001/DATA/ (accessed on 4 September 2023). The MRAMS mesoscale atmospheric model is installed at the Southwest Research Institute in Boulder (Boulder, CO, USA). https://www.boulder.swri.edu/~rafkin/ (accessed on 4 September 2023).

Acknowledgments: Thanks to the members of NASA's Mars Science Laboratory mission, through which studies such as this one can be carried out, thus allowing for the advancement of global science knowledge. Part of this work was carried out at the Jet Propulsion Laboratory/California Institute of Technology under a grant from NASA-STMD, and under a contract with the National Aeronautics and Space Administration (80NM0018D0004).

Conflicts of Interest: The authors declare no conflicts of interest.

Appendix A

Table A1. Maximum and minimum atmospheric pressure values by years.

P_{atm}	MY-31	MY-32	MY-33	MY-34	MY-35	MY-36	MY-37
min (K)	688.88	688.41	686.6	670.44	664.92	654.84	684.82
Ls (°)	162.6	162.7	154.2	151.2	159.5	155.3	124.6
alt (m)	−4502.36	−4460.45	−4431.27	−4161.67	−4094.76	−3956.02	−3767.88
ΔZ (m)	18.947	60.855	90.041	359.641	426.551	565.291	753.431
sol	22	691	1344	2007	2691	3351	3960
max (K)	969.13	959.15	940.89	928.73	925.93	911.86	878.74
Ls (°)	248.3	268.6	234.4	244.4	243.3	250.9	58.0
alt (m)	−4520.36	−4459.77	−4368.81	−4150.12	−4128.68	−3909.96	−3826.55
ΔZ (m)	0.942	61.534	152.501	371.191	392.631	611.351	694.761
sol	163	862	1478	2163	2829	3509	3815

Registration of the calculated values for the atmospheric pressure (P_{atm}) of the 3967 sols studied, classifying them by Martian year (MY). The values provided being the following: min and max: the minimum and maximum pressures; Ls: solar longitude; alt: altitude; ΔZ: elevation with respect to the landing point; and sol: the exact sol on which the above values occur.

Table A2. Maximum and minimum atmospheric temperature values by years.

T_{atm}	MY-31	MY-32	MY-33	MY-34	MY-35	MY-36	MY-37
min (K)	190.69	185.77	186.14	192.40	191.49	192.72	191.28
Ls (°)	355.6	78.4	94.4	82.5	93.1	55.4	86.5
alt (m)	−4501.17	−4487.28	−4423.76	−4174.66	−4129.78	−4067.48	−3811.28
ΔZ (m)	20.137	34.025	97.551	346.651	391.531	453.831	710.031
sol	329	535	1243	1721	2422	3642	3724
max (K)	269.53	276.45	276.90	272.19	272.79	276.51	262.34
Ls (°)	248.9	194.6	204.7	173.0	218.2	219.4	6.7
alt (m)	−4520.5	−4460.94	−4403.79	−4188.74	−4109.67	−3961.07	−3862.56
ΔZ (m)	0.811	60.366	117.521	332.571	411.641	560.241	658.751
sol	164	747	1432	2047	2790	3461	3706

Registration of the calculated values for the atmospheric temperature (T_{atm}) of the 3967 sols studied, classifying them by Martian year (MY). The values provided being the following: min and max: the minimum and maximum pressures; Ls: solar longitude; alt: altitude; ΔZ: elevation with respect to the landing point; and sol: the exact sol on which the above values occur.

Table A3. Maximum and minimum surface temperature values by years.

T_{surf}	MY-31	MY-32	MY-33	MY-34	MY-35	MY-36	MY-37
min (K)	185.63	171.74	175.30	174.07	154.02	175.12	175.33
Ls (°)	348.4	85.9	104.2	16.8	32.6	332.7	15.4
alt (m)	−4515.41	−4487.81	−4423.52	−4255.55	−4154.23	−3860.34	−3856.78
ΔZ (m)	5.899	33.495	97.791	265.761	367.081	660.971	664.531
sol	329	535	1243	1721	2422	3642	3724
max (K)	287.93	288.48	289.37	286.14	289.98	293.16	275.19
Ls (°)	214.4	173.4	202.3	175.8	213.9	212.1	3.8
alt (m)	−4518.23	−4458.24	−4407.72	−4190.05	−4104.15	−3965.25	−3861.09
ΔZ (m)	3.076	63.068	113.591	331.261	417.161	556.061	660.221
sol	111	711	1428	2052	2783	3449	3700

Registration of the calculated values for the surface temperature (T_{surf}) of the 3967 sols studied, classifying them by Martian year (MY). The values provided being the following: min and max: the minimum and maximum pressures; Ls: solar longitude; alt: altitude; ΔZ: elevation with respect to the landing point; and sol: the exact sol on which the above values occur.

References

1. Hughes, J.; Ross, A.; Vosper, S.; Lock, A.; Jemmett-Smith, B. Assessment of valley cold pools and clouds in a very high-resolution numerical weather prediction model. *Geosci. Model Dev.* **2015**, *8*, 3105–3117. [CrossRef]
2. Rasilla, D.; Martilli, A.; Allende Álvarez, F.; Fernandez, F. Long term evolution of cold air pools (CAPs) over the Madrid basin. *Int. J. Climatol.* **2022**, *43*, 2055–2067. [CrossRef]

3. Bacer, S.; Beaumet, J.; Ménégoz, M.; Gallée, H.; Bouëdec, E.; Staquet, C. Impact of climate change on persistent cold-air pools in an alpine valley during the 21st century. *EGU Gen. Assem.* **2023**. [CrossRef]
4. Larsen, S.; Jørgensen, H.; Landberg, L.; Tillman, J. Aspects of the atmospheric surface layers on Mars and Earth. *Bound. Layer Meteorol.* **2002**, *105*, 451–470. [CrossRef]
5. Grotzinger, J.P.; Crisp, J.; Vasavada, A.R.; Anderson, R.C.; Baker, C.J.; Barry, R.; Blake, D.F.; Conrad, P.; Edgett, K.S.; Ferdowski, B.; et al. Mars Science Laboratory Mission and Science Investigation. *Space Sci. Rev.* **2012**, *170*, 5–56. [CrossRef]
6. Petrosyan, A.; Galperin, B.; Larsen, S.E.; Lewis, S.R.; Määttänen, A.; Read, P.L.; Rennó, N.; Rogberg, L.P.; Savijärvi, H.; Siili, T.; et al. The Martian atmospheric boundary layer. *Rev. Geophys.* **2011**, *49*, RG3005. [CrossRef]
7. Tillman, J.E. Mars global atmospheric oscillations: Annually synchronized, transient normal-mode oscillations and the triggering of global dust storms. *J. Geophys. Res.* **1988**, *93*, 9433–9451. [CrossRef]
8. Eckert, M. The Boundary Layer Concept. In *Turbulence—An Odyssey. History of Physics*; Springer: Cham, Switzerland, 2022. [CrossRef]
9. Spiga, A. The planetary boundary layer of Mars. *Oxf. Res. Encycl. Planet. Sci.* **2024**.
10. Pascal, B. *Oeuvres Complètes*; Périer to Pascal, 22 September 1648; Seuil: Paris, France, 1960; Volume 2, p. 682.
11. Howari, F.M.; Sharma, M.; Nazzal, Y.; Barbulescu, A.; Alaydaroos, F.; Xavier, C.M. Atmospheric Topographic Analysis of a Part of Mars. *Rom. Rep. Phys.* **2021**, *73*, 805.
12. Savijärvi, H.; Harri, A.M.; Kemppinen, O. The diurnal water cycle at Curiosity: Role of exchange with the regolith. *Icarus* **2015**, *265*, 261–274. [CrossRef]
13. Dundas, C.M.; Becerra, P.; Byrne, S.; Chojnacki, M.; Daubar, I.J.; Diniega, S.; Hansen, C.J.; Herkenhoff, K.E.; Landis, M.E.; McEwen, A.S.; et al. Active Mars: A Dynamic World. *J. Geophys. Res. Planets* **2021**, *126*, e2021JE006876. [CrossRef]
14. Gómez-Elvira, J.; Armiens, C.; Castañer, L.; Domínguez, M.; Genzer, M.; Gómez, F.; Haberle, R.; Harri, A.M.; Jiménez, V.; Kahanpää, H.; et al. REMS: The Environmental Sensor Suite for the Mars Science Laboratory Rover. *Space Sci. Rev.* **2012**, *170*, 583–640. [CrossRef]
15. Gómez-Elvira, J.; Armiens, C.; Carrasco, I.; Genzer, M.; Gómez, F.; Haberle, R.V. Curiosity's rover environmental monitoring station. *Space Sci. Rev.* **2014**, *170*, 583–640. [CrossRef]
16. Newman, C.; Gómez-Elvira, J.; Marin, M.; Navarro, S.; Torres, J.; Richardson, M.I.; Battalio, J.M.; Guzewich, S.D.; Sullivan, R.; Torre-Juárez, M.; et al. Winds measured by the Rover Environmental Monitoring Station (REMS) during the Mars Science Laboratory (MSL) rover's Bagnold Dunes Campaign and comparison with numerical modeling using MarsWRF. *Icarus* **2017**, *291*, 203–231. [CrossRef]
17. Sebastián, E.; Armiens, C.; Gómez-Elvira, J.; Zorzano, M.P.; Martínez-Frías, J.; Esteban, B.; Ramos, M. The Rover Environmental Monitoring Station Ground Temperature Sensor: A pyrometer for measuring ground temperature on Mars. *Sensors* **2010**, *10*, 921–931. [CrossRef] [PubMed]
18. García Muñoz, R.; Forget, F.; Ochoa, J.L.F. The Rover Environmental Monitoring Station (REMS) for the Mars Science Laboratory (MSL). *Space Sci. Rev.* **2012**, *170*, 583–640.
19. Harri, A.M.; Genzer, M.; Kemppinen, O.; Gomez-Elvira, J.; Haberle, R.; Polkko, J.; Savijärvi, H.; Rennó, N.; Rodriguez-Manfredi, J.A.; Schmidt, W.; et al. Mars Science Laboratory relative humidity observations: Initial results. *J. Geophys. Res. Planets* **2013**, *119*, 2132–2147. [CrossRef] [PubMed]
20. Rafkin, S.; Robert, M.; Haberle, R.; Michaels, T. The Mars Regional Atmospheric Modeling System: Model description and selected simulations. *Icarus* **2001**, *151*, 228–256. [CrossRef]
21. Rafkin, S.; Michaels, T. The Mars Regional Atmospheric Modeling System (MRAMS): Current status and future directions. *Atmosphere* **2019**, *10*, 747. [CrossRef]
22. Pla-Garcia, J.; Rafkin, S.C. The Meteorology of Gale Crater as Determined from Rover Environmental Monitoring Station Observations and Numerical Modeling. Part I: Comparison of Model Simulations with Observations. *Icarus* **2016**, *280*, 103–113. [CrossRef]
23. Torre-Juárez, M.; Piqueux, S.; Kass, D.; Newman, C.; Guzewich, S. Pressure deficit in Gale Crater and a larger northern polar cap after the MY34 global dust storm. *J. Geophys. Res. Planets* **2024**, *129*, e2023JE007810. [CrossRef]
24. Tillman, J.E.; Johnson, N.C.; Guttorp, P.; Percival, D.B. The Martian annual atmospheric pressure cycle: Years without great dust storms. *J. Geophys. Res.* **1993**, *98*, 10963–10971. [CrossRef]
25. Viúdez-Moreiras, D.; Newman, C.E.; De la Torre, M.; Martínez, G.; Guzewich, S.; Lemmon, M.; Pla-García, J.; Smith, M.D.; Harri, A.M.; Genzer, M.; et al. Effects of the MY34/2018 global dust storm as measured by MSL REMS in Gale Crater. *J. Geophys. Res. Planets* **2019**, *124*, 1899–1912. [CrossRef] [PubMed]
26. Martínez, G.M.; Torre-Juárez, M.; Vicente-Retortillo, Á.; Kemppinen, O.; Rennó, N.; Lemmon, M. Análisis de las condiciones ambientales en el cráter Gale en el marco de la misión MSL. *Boletín Geofísico* **2016**, *39*, 5–14.
27. Pál, B.; Kereszturi, Á.; Forget, F.; Smith, M.D. Global Seasonal Variations of the Near-Surface Relative Humidity Levels on Present-Day Mars. *Icarus* **2019**, *333*, 481–495. [CrossRef]

28. Martínez, G.M.; Vicente-Retortillo, A.; Vasavada, A.R.; Newman, C.E.; Fischer, E.; Rennó, N.O.; Savijärvi, H.; de la Torre, M.; Ordóñez-Etxeberria, I.; Lemmon, M.T.; et al. The Surface Energy Budget at Gale Crater During the First 2500 Sols of the Mars Science Laboratory Mission. *J. Geophys. Res. Planets* **2021**, *126*, e2020JE006804. [CrossRef]
29. Schofield, J.T.; Crisp, D.; Barnes, J.R.; Haberle, R.M.; Magalhães, J.A.; Murphy, J.R.; Seiff, A.; Larsen, S. The Mars Pathfinder Atmospheric Structure Investigation/Meteorology (ASI/MET) Experiment. *Science* **1997**, *278*, 1752–1758. [CrossRef]
30. Smith, M.D.; Wolff, M.J.; Lemmon, M.T.; Spanovich, N.; Banfield, D.; Budney, C.J.; Clancy, R.T.; Ghosh, A.; Landis, G.A.; Smith, P.; et al. First Atmospheric Science Results from the Mars Exploration Rover's Mini-TES. *Science* **2005**, *310*, 298–303. [CrossRef]
31. Rafkin, S.C.; Pla-Garcia, J.; Kahre, M.; Gómez-Elvira, J.; Hamilton, V.E.; Marín, M.; Vasavada, A. The Meteorology of Gale Crater as Determined from Rover Environmental Monitoring Station Observations and Numerical Modeling. Part II: Interpretation. *Icarus* **2016**, *280*, 114–138. [CrossRef]
32. Blackburn, D.; Bryson, K.; Chevrier, V.; Roe, L.; Hook, K. Sublimation Kinetics of CO2 Ice on Mars. *Planet. Space Sci.* **2010**, *58*, 780–791. [CrossRef]
33. Thomas, N.; Hansen, C.; Pommerol, A.; Portyankina, G.; Aye, K.M.; Russell, P. Observations of the Surface Effects of the CO2 and H_2O Cycles on Mars. In Proceedings of the European Space Agency (ESA) Symposium on Mars Exploration, Valencia, Spain, 9–13 July 2013; pp. 57–70.
34. Forget, F.; Hourdin, F.; Fournier, R.; Hourdin, C.; Talagrand, O.; Collins, M.; Lewis, S.R.; Read, P.L.; Huot, J.P. Improved General Circulation Models of the Martian Atmosphere from the Surface to Above 80 km. *J. Geophys. Res.* **1999**, *104*, 24155–24175. [CrossRef]
35. Millour, E.; Forget, F.; Spiga, A.; Vals, M.; Zakharov, V.; Montabone, L.; Lefèvre, F.; Montmessin, F.; Chaufray, J.-Y.; López-Valverde, M.A.; et al. The Mars Climate Database (Version 5.3). *Sci. Workshop Mars Express ExoMars* **2018**, *68*.
36. Guzewich, S.D.; Lemmon, M.; Smith, C.L.; Martínez, G.; de Vicente-Retortillo, Á.; Newman, C.E.; Baker, M.; Campbell, C.; Cooper, B.; Gómez-Elvira, J.; et al. Mars Science Laboratory Observations of the 2018/Mars Year 34 Global Dust Storm. *Geophys. Res. Lett.* **2019**, *46*, 71–79. [CrossRef]
37. Guzewich, S.D.; Fedorova, A.A.; Kahre, M.A.; Toigo, A.D. Studies of the 2018/Mars Year 34 Planet-Encircling Dust Storm. *J. Geophys. Res. Planets* **2020**, *125*, e2020JE006700. [CrossRef]
38. Chen-Chen, H.; Pérez-Hoyos, S.; Sanchez-Lavega, A. Dust Particle Size, Shape, and Optical Depth During the 2018/MY34 Martian Global Dust Storm Retrieved by MSL Curiosity Rover Navigation Cameras. *Planet. Space Sci.* **2020**, *180*, 104746. [CrossRef]
39. Lapotre, M.G.; Ewing, R.C.; Lamb, M.P.; Fischer, W.W.; Grotzinger, J.P.; Rubin, D.M.; Lewis, K.W.; Ballard, M.J.; Day, M.; Gupta, S.; et al. Large Wind Ripples on Mars: A Record of Atmospheric Evolution. *Science* **2016**, *353*, 55–58. [CrossRef]
40. Vasavada, A.; Piqueux, S.; Lewis, K.; Lemmon, M.; Smith, M. Thermophysical Properties along Curiosity's Traverse in Gale Crater, Mars, Derived from the REMS Ground Temperature Sensor. *Icarus* **2017**, *284*, 373–384. [CrossRef]
41. Gendrin, A.; Mangold, N.; Bibring, J.P.; Langevin, Y.; Gondet, B.; Poulet, F.; Bonello, G.; Quantin, C.; Mustard, J.; Arvidson, R.; et al. Sulfates in Martian Layered Terrains: The OMEGA/Mars Express View. *Science* **2005**, *307*, 1587–1591. [CrossRef] [PubMed]
42. Bakker, W.; Ruitenbeek, F.J.A.; van der Werff, H.; Zegers, T.E.; Oosthoek, J.; Marsh, S.; Meer, F.D. Processing OMEGA/Mars Express Hyperspectral Imagery from Radiance-at-Sensor to Surface Reflectance. *Planet. Space Sci.* **2013**, *90*, 1–9. [CrossRef]
43. Christensen, P.R.; Bandfield, J.L.; Hamilton, V.E.; Ruff, S.W.; Kieffer, H.H.; Titus, T.N.; Malin, M.C.; Morris, R.V.; Lane, M.D.; Clark, R.L.; et al. Mars Global Surveyor Thermal Emission Spectrometer Experiment: Investigation Description and Surface Science Results. *J. Geophys. Res.* **2001**, *106*, 23823–23871. [CrossRef]
44. Montmessin, F.; Forget, F.; Rannou, P.; Cabane, M.; Haberle, R.M. Origin and Role of Water Ice Clouds in the Martian Water Cycle as Inferred from a General Circulation Model. *J. Geophys. Res.* **2004**, *109*, E10004. [CrossRef]
45. Clancy, R.T.; Grossman, A.W.; Wolff, M.J.; James, P.B.; Rudy, D.J.; Billawala, Y.N.; Sandor, B.J.; Lee, S.W.; Muhleman, D.O. Water Vapor Saturation at Low Altitudes Around Mars Aphelion: A Key to Mars Climate? *Icarus* **1996**, *122*, 36–62. [CrossRef]
46. Fedorova, A.A.; Montmessin, F.; Korablev, O.; Luginin, M.; Trokhimovskiy, A.; Belyaev, D.A.; Ignatiev, N.I.; Lefèvre, F.; Alday, J.; Irwin, P.G.; et al. Stormy Water on Mars: The Distribution and Saturation of Atmospheric Water During the Dusty Season. *Science* **2020**, *397*, 297–300. [CrossRef]
47. Maltagliati, L.; Montmessin, F.; Fedorova, A.; Korablev, O.; Forget, F.; Bertaux, J.-L. Evidence of Water Vapor in Excess of Saturation in the Atmosphere of Mars. *Science* **2011**, *333*, 1868–1871. [CrossRef]
48. Carrozzo, F.G.; Bellucci, G.; Altieri, F.; D'Aversa, E.; Bibring, J.-P. Mapping of Water Frost and Ice at Low Latitudes on Mars. *Icarus* **2009**, *203*, 406–420. [CrossRef]
49. Poncin, L.; Kleinböhl, A.; Kass, D.; Clancy, R.; Aoki, S.; Vandaele, A. Water Vapor Saturation and Ice Cloud Occurrence in the Atmosphere of Mars. *Planet. Space Sci.* **2021**, *212*, 105390. [CrossRef]
50. Leovy, C.B.; Smith, B.A.; Young, A.T.; Leighton, R.B. Mariner Mars 1969: Atmospheric Results. *J. Geophys. Res.* **1971**, *76*, 297–312. [CrossRef]
51. Smith, I.B.; Spiga, A. Seasonal Variability in Winds in the North Polar Region of Mars. *Icarus* **2018**, *308*, 188–196. [CrossRef]

52. Lemmon, M.T.; Wolff, M.J.; Bell, J.F., III; Smith, M.D.; Cantor, B.A.; Smith, P.H. Dust Aerosol, Clouds, and the Atmospheric Optical Depth Record Over 5 Mars Years of the Mars Exploration Rover Mission. *Icarus* **2014**, *231*, 323–343. [CrossRef]
53. Basu, S.; Wilson, J.; Richardson, M.; Ingersoll, A. Simulation of Spontaneous and Variable Global Dust Storms with the GFDL Mars GCM. *J. Geophys. Res.* **2006**, *111*, E09004. [CrossRef]
54. Zalucha, A. The Effect of Dust on the Martian Hadley Cells in the Presence of Topography at Equinox. *Geophys. Res. Lett.* **2011**, *38*, L15203.
55. Lee, C.; Lawson, W.; Richardson, M.; Heavens, N.; Kleinböhl, A.; Banfield, D.; McCleese, D.; Zurek, R.; Kass, D.; Schofield, J.; et al. Thermal Tides in the Martian Middle Atmosphere as Seen by the Mars Climate Sounder. *J. Geophys. Res.* **2009**, *114*, E01007. [CrossRef] [PubMed]
56. Lee, C.; Lawson, W.; Richardson, M.; Heavens, N.; McCleese, D.; Banfield, D. Thermal Tides in the Martian Middle Atmosphere. *AGU Fall Meet. Abstr.* **2008**, *2008*, P51B-1411.
57. Guzewich, S.; Newman, C.; Torre-Juarez, M.; Wilson, R.; Lemmon, M.; Smith, M.D.; Kahanpää, H.; Harri, A.M. Atmospheric Tides in Gale Crater, Mars. *Icarus* **2015**, *268*, 37–49. [CrossRef]
58. Richardson, M.I.; Newman, C.E. On the Relationship Between Surface Pressure, Terrain Elevation, and Air Temperature. Part I: The Large Diurnal Surface Pressure Range at Gale Crater, Mars and Its Origin Due to Lateral Hydrostatic Adjustment. *Planet. Space Sci.* **2018**, *164*, 132–157. [CrossRef]

Disclaimer/Publisher's Note: The statements, opinions and data contained in all publications are solely those of the individual author(s) and contributor(s) and not of MDPI and/or the editor(s). MDPI and/or the editor(s) disclaim responsibility for any injury to people or property resulting from any ideas, methods, instructions or products referred to in the content.